

JGR Atmospheres

RESEARCH ARTICLE

10.1029/2020JD033956

Key Points:

- The mean annual mass balance was -0.39 m w.e. a^{-1} and point mass balance below 6,070 m a.s.l. was always negative during the 2011–2018 period
- Annual precipitation controlled the changes in annual mass balance mainly through changing ablation-season albedo and melt energy
- The reduced mass loss rates in the western Himalayas during the last two decades were partly explained by increasing annual precipitation

Supporting Information:

Supporting Information may be found in the online version of this article.

Correspondence to:

H. Zhao,
zhaohb@itpcas.ac.cn

Citation:

Zhu, M., Yang, W., Yao, T., Tian, L., Thompson, L. G., & Zhao, H. (2021). The influence of key climate variables on mass balance of Naimona'nyi glacier on a north-facing slope in the western Himalayas. *Journal of Geophysical Research: Atmospheres*, 126, e2020JD033956. <https://doi.org/10.1029/2020JD033956>





Received 24 SEP 2020

Accepted 4 MAR 2021

Author Contributions:

Conceptualization: Tandong Yao
Data curation: Huabiao Zhao
Formal analysis: Meilin Zhu, Wei Yang, Tandong Yao, Lide Tian, Huabiao Zhao
Funding acquisition: Meilin Zhu, Wei Yang, Tandong Yao, Lonnie G. Thompson, Huabiao Zhao
Investigation: Lide Tian, Huabiao Zhao
Methodology: Meilin Zhu, Wei Yang
Validation: Meilin Zhu
Visualization: Meilin Zhu
Writing – original draft: Meilin Zhu
Writing – review & editing: Wei Yang, Lide Tian, Lonnie G. Thompson

The Influence of Key Climate Variables on Mass Balance of Naimona'nyi Glacier on a North-Facing Slope in the Western Himalayas

Meilin Zhu^{1,2} , Wei Yang^{1,3}, Tandong Yao^{1,3}, Lide Tian^{3,4} , Lonnie G. Thompson² , and Huabiao Zhao^{1,3,5} 

¹Key Laboratory of Tibetan Environment Changes and Land Surface Processes, Institute of Tibetan Plateau Research, Chinese Academy of Sciences (CAS), Beijing, China, ²Byrd Polar and Climate Research Center, The Ohio State University, Columbus, OH, USA, ³CAS Center for Excellence in Tibetan Plateau Earth Sciences, CAS, Beijing, China, ⁴Institute of International Rivers and Eco-security, Yunnan University, Kunming, China, ⁵Ngari Station for Desert Environment Observation and Research, Institute of Tibetan Plateau Research, CAS, Tibet, China

Abstract Glacier mass changes in the Himalayas impact on sustainable water resources and hazards in downstream regions. However, mass balance variation and its drivers on north-facing slopes in the Himalayas are not well understood. This study presents the meteorological conditions, energy and mass balance characteristics for Naimona'nyi Glacier on a north-facing slope in the western Himalayas, based on energy-mass balance model and high-altitude measurements from October 2010 to September 2018. The average annual mass balance measured for Naimona'nyi Glacier was -0.39 m water equivalent a^{-1} and point mass balances below 6,070 m above sea level were always negative. Simulations showed that melt during the ablation season dominated the annual mass balance and the interannual variability in the mass balance, and that variability in melt energy was controlled by albedo during the ablation season. The annual mass balance was found to be significantly correlated with annual precipitation during the 2011–2018 period, which is accounted for by the change in ablation-season albedo and melt energy. The average mass balance for glaciers in the western Himalayas were higher during the 2010–2019 period than during the 2000–2009 period, partly because of higher annual precipitation during the 2010–2019 period. Over the last 20 years, the increased precipitation in the cold season was driven by a cyclonic circulation anomaly over the northwestern Indian Peninsula, which may be linked to the strengthened North Atlantic Oscillation, and the increased precipitation in the ablation season was driven by an anomaly in the cyclonic circulation over Central India, which may be related to enhanced deep convection over the Indian subcontinent and the enhanced Atlantic multidecadal oscillation.

1. Introduction

Glacier mass changes in the Himalayas are a subject of societal concern due to their impact on many large Asian rivers that are relied upon for sustainable water resources (Immerzeel et al., 2020; Wang et al., 2015; Yao et al., 2019); their effect on hazards in downstream regions such as glacial lake outburst floods (Carrivick & Tweed, 2016); and their effect on the availability of Himalayan paleoclimate records from ice cores (Kehrwald et al., 2008; Thompson et al., 2011). Recent studies show that Himalayan glaciers have experienced rapid thinning and shrinkage and that the rates of observed mass changes are spatially and temporally variable (Azam et al., 2014; Bolch et al., 2012; Brun et al., 2017; Maurer et al., 2019; Shean et al., 2020; Yao et al., 2012). The drivers for the spatiotemporal variability are not well understood and a variety of factors have been proposed to explain it, including debris cover (Scherler et al., 2011), glacier-lake interactions (King et al., 2018), morphological variables (Brun et al., 2019), climate variability (patterns in air temperature, precipitation, and atmospheric circulation) and the response of individual glaciers to climate variability (Forsythe et al., 2017; Fujita & Nuimura, 2011; Sakai & Fujita, 2017; Yao et al., 2012).

To enhance our current understanding of the spatiotemporal variability of mass balance for glaciers across the Himalayas, it is important to explore the mechanisms that control changes in mass balance for some typical Himalayan glaciers (Fujita & Nuimura, 2011; Yao et al., 2012). The relevant studies mainly focused on the south-facing slopes in the Himalayas (Azam et al., 2014; Bonekamp et al., 2019; Sherpa et al., 2017; Sunako et al., 2019; Wagnon et al., 2013). For example, Sunako et al. (2019) looked at Trambau Glacier, on

a south-facing slope in the central Himalaya and found significant correlation between annual mass balance and annual precipitation, but no discernible correlation between annual mass balance and summer mean air temperature, while Mandal et al. (2020) found that interannual variability for the mass balance of Chhota Shigri Glacier, on a south-facing slope in the western Himalayas, was driven by variations in air temperature during the ablation season (June to September). These studies demonstrate that the climate variables that drive changes to glacier mass balance vary spatially across the Himalayas, possibly reflecting a different glacier response where the background climate is different (Sakai & Fujita, 2017; Zhu, Yao, Yang, Xu, Wu, & Wang, 2018).

To improve our understanding of Himalayan glacier behavior, particularly for glaciers on north-facing slopes, which experience different climate conditions to south-facing slopes (Bookhagen et al., 2010; Mausson et al., 2014), further research into the mechanisms that determine changes in mass balance for glaciers in different regions of the Himalayas is needed. There are few in-situ observations of meteorology and glaciology available for high altitudes on north-facing slopes in the Himalayas. This makes it difficult to investigate relationships between climate variables (e.g., air temperature and precipitation) and glacier mass balance, and to analyze the influence of atmospheric circulation on changes to glacier mass balance (e.g., Mölg et al., 2014; Yang et al., 2016; Zhu, Yao, Yang, Xu, Wu, Wang, & Xie, 2018).

In-situ high-altitude meteorological and glaciological observations can be used with the energy-mass balance (EMB) model to describe the physical processes of glacier accumulation and ablation and to quantify the influence of climate factors on changes to glacier mass balance (Huint, 2014; Mölg et al., 2014; Yang et al., 2013; Zhu et al., 2015). Naimona'nyi Glacier is on a north-facing slope in the western Himalayas and is the subject of an established long-term meteorological and glaciological monitoring campaign (Tian et al., 2014; Yao et al., 2012; Zhao et al., 2016). Based on a degree-day model and meteorological data from Burang meteorological station, Zhao et al. (2016) showed that the average annual mass loss increased from $\sim 0.01 \pm 0.15$ m water equivalent (w.e.) a^{-1} during the 1974–1983 period to $\sim 0.69 \pm 0.21$ m w.e. a^{-1} during the 2004–2014 period due to the dramatic temperature increase and simultaneous significant precipitation decrease that began the late 1980s. Their study focused on the qualitative analysis about the relationship between local climate factors and the accelerated mass loss on the interdecadal scales. The temporal changes in mass balance and possible relationships with local and regional climate variables should be investigated further. Based on energy and mass balance model, and new mass balance and meteorological data from Naimona'nyi Glacier for 2010–2018, we aim to: 1) characterize the energy and mass balance characteristics of Naimona'nyi Glacier, the meteorology it experiences, and the temporal variability of these; 2) analyze the relationship between the mass balance and local climate factors, to understand what drives changes to mass balance on north-facing slopes in the western Himalayas and to gain insights into the macroscale atmospheric circulation patterns that may affect glacier mass changes in the western Himalayas; 3) compare the mass balance for Naimona'nyi Glacier with that for other glaciers across the Himalayas over the last 10 years and to identify potential drivers for any spatial differences. This study will improve our understanding of glacier behaviors and their relationships with the regional circulation on north-facing slopes in the western Himalayas, and lead to advances in understanding of spatial and temporal differences in glacier mass changes across the Himalayas.

2. Study Area, Method, and Data

2.1. Study Area

Naimona'nyi Glacier is a typical sub-continental (Shi & Liu, 2000), valley-type glacier. It is located on a north-facing slope in the western Himalayas, on the southwestern Tibetan Plateau (TP) and has two branches (Figure 1). In this work, we focused on the northern branch. The upper part of the glacier has a smooth surface, while the surface for the lower part is rough due to surface melt. There are very few debris in the terminus of the glacier. The area of the glacier is 7.34 km^2 and it ranges in altitude from $\sim 5,545$ to $7,261.5$ m above sea level (a.s.l.) (Guo et al., 2015). More than 90% of the glacier's area is below 6,200 m a.s.l. and half of the area is between 6,000 and 6,200 m a.s.l. (Figure 1b). The maximum thickness of this glacier exceeds 250 m (Tian et al., 2014). The area of Naimona'nyi glacier has decreased by $\sim 0.8 \text{ km}^2$ between 2003 and 2013 (Zhu et al., 2014), and the average mass balance of the reconstructed time series from October 1973 to September 2013 was -0.4 m w.e. a^{-1} (Zhao et al., 2016). Burang meteorological station ($30^{\circ}17'N$,

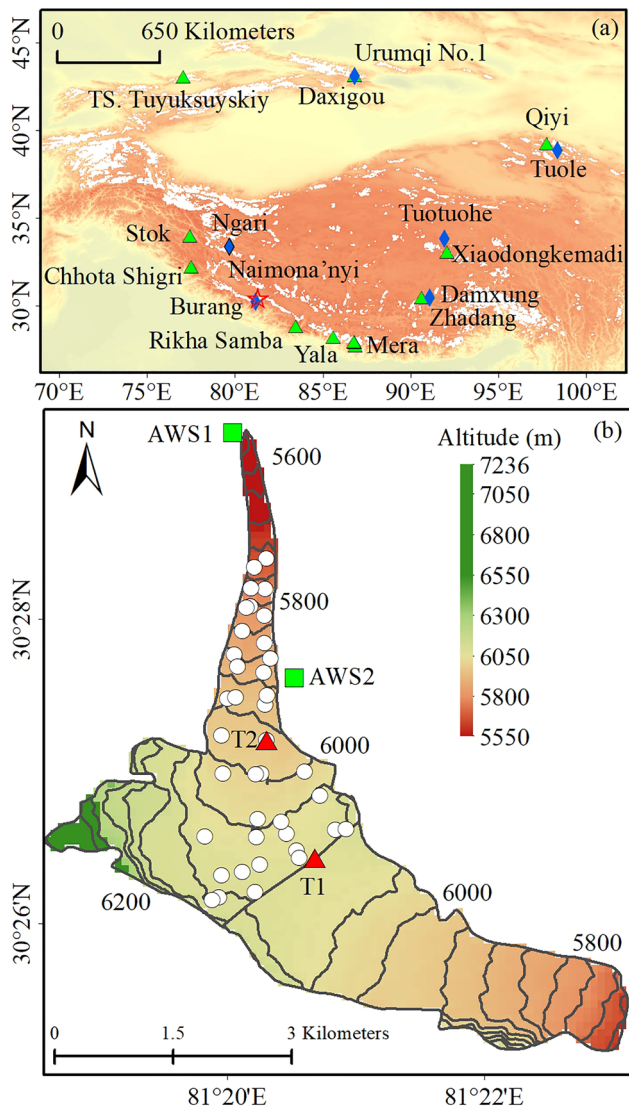


Figure 1. (a) Locations of Naimona'nyi Glacier (red star), 12 selected glaciers with continuous mass balance measurements (green triangles) and six meteorological stations (blue diamond). Please note that Mera indicated three glaciers, Mera, Changri Nup and Pokalde glaciers; (b) a contour map with the distribution of surface mass balance stakes (white dots) in October 2010 on Naimona'nyi Glacier, the two AWSs (green square) and two air temperature and humidity probes (red triangles, T1 and T2).

AWS1 were interrupted. AWS2 was installed at 5,950 m a.s.l. in October 2010 and recorded T_a , RH, S_{in} , WS, and WD at hourly resolution. There is a gap in all measurements recorded at AWS2 from April 2012 to September 2012, and a gap in T_a and RH recorded at AWS2 from January 2013 to September 2013 due to the air temperature and humidity probe at AWS2 falling out of its solar radiation shield. Precipitation data was obtained from all-weather precipitation gauges (T-200B) equipped with hanging weighing transducers installed close to AWS2 in September 2013. Two air temperature and humidity sensors (T1 and T2) were installed on Naimona'nyi Glacier in October 2018 at 6,075 and 5,984 m a.s.l., respectively, to measure gradients in air temperature and relative humidity (Figure 1b). Details of the instruments used for the meteorological observations are listed in Table S1.

81°15'E, 3,900 m a.s.l.), located ~20 km from Naimona'nyi Glacier (Figure 1a), shows that the average air temperature is 3.6°C, with highest mean monthly air temperature occurring in July and August, and that the annual precipitation cycle follows a bimodal distribution, and the annual average precipitation is 163.2 mm (Figure S1).

2.2. Field Measurements and Data Processing

2.2.1. Mass Balance Measurements

The mass balance was measured using the glaciological method for the northern branch of Naimona'nyi Glacier since 2004. In this work, we focused on the periods from October 2010 to September 2018 because available in-situ meteorological observations started from 2010. In October 2010, 39 monitoring stakes were drilled into the ice, distributed across the entire glacier surface (Figure 1b). Some stakes were lost due to glacier surface melt, or were damage by animals, and some measurements failed due to extremely bad weather. Despite this, our observation network provided a minimum of 15 point measurements of mass balance for 2013/14 (October 2013 to September 2014). Due to logistical issues, no fieldwork was carried out in 2015, but point measurements of mass balance were obtained in October 2016, and these can be used to calculate glacier-wide mass balance over the longer period of 2014/16 (October 2014 to September 2016). The stakes were located between 5,750 and 6,130 m a.s.l. (Figure 1b). In early October for each year of the study, we manually recorded the stake heights and snow-pit features (snow layer density and stratigraphy) to derive the annual point mass balance. The annual glacier-wide mass balance B_a (m w.e.) is calculated according to:

$$B_a = \frac{\sum_{i=1}^n B_i S_i}{\sum_{i=1}^n S_i}, \quad (1)$$

where n is the total number of altitude intervals for Naimona'nyi Glacier; S_i (m^2) is the area for each interval; B_i (m w.e.) is the point mass balance at the middle altitude at each individual interval, which is calculated by the interpolation and extrapolation of the point mass balance at stakes.

2.2.2. Meteorological Measurements

Two automatic weather stations (AWSs) were installed on a lateral moraine beside Naimona'nyi Glacier (Figure 1b). AWS1, at 5,543 m a.s.l., recorded meteorological variables from October 2011 at half hourly resolution, including air temperature (T_a), relative humidity (RH), and downward shortwave radiation (S_{in}). The data of incoming longwave radiation (L_{in}), net radiation (R_{net}), wind speed (WS), and wind direction (WD) at

2.3. Other Data

Monthly air temperature and precipitation from six meteorological stations (Table S2) were used in addition to the above, to discuss the relationship between glacier mass balance and climate factors for different regions on the TP (Figure 1a). We also used monthly geopotential height and wind fields at 500 hPa levels, air temperature at 2 m and total precipitation from the fifth generation of reanalysis data from the European Center for Medium-Range Weather Forecasts (ERA5) to assess changes to glacier mass balance in the context of macroscale atmospheric circulation. The ERA5 data have a horizontal resolution of $0.25^\circ \times 0.25^\circ$ and have been widely used in climate research (Hoffmann et al., 2019; von Engeln & Teixeira, 2013).

3. Method

3.1. The Energy and Mass Balance Model

The EMB model used in this study is described in detail in Fujita and Ageta (2000) and Yang et al. (2013). Here, we only summarize the main features of the EMB model. The model solves the following equation for the point mass balance (MB):

$$\text{MB} = \int \left(\frac{Q_M}{L_m} + \frac{H_{\text{lat}}}{L_v} + C_{\text{en}} + P_{\text{snow}} \right) dt, \quad (2)$$

where MB is the net of surface melt, sublimation (or evaporation), refreezing (C_{en}) and snowfall (P_{snow}). L_m is the latent heat of ice melt and L_v is the latent heat of evaporation or sublimation. Melt energy (Q_M) is calculated using the surface energy balance equation:

$$Q_M = S_{\text{in}}(1 - \alpha) + L_{\text{in}} + L_{\text{out}} + H_{\text{sen}} + H_{\text{lat}} + Q_G, \quad (3)$$

Where α is the albedo; L_{out} is the outgoing longwave radiation; H_{sen} and H_{lat} are the sensible and latent heat fluxes, respectively; Q_G is the conductive heat flux. Q_M is defined as positive. Except Q_M , all fluxes are defined as positive when directed toward the surface. The description about α , L_{in} , L_{out} , turbulent heat fluxes, Q_G , refreezing, and snowfall were summarized in Appendix A. The parameters of the EMB model were presented in Table S3.

The time series of daily mean T_a , daily mean RH and daily mean S_{in} from AWS1, and daily mean WS and daily total precipitation from AWS2, were used to drive the EMB model to simulate the glacier mass balance at 40 m altitude intervals. These meteorological variables, except WS, were interpolated to each elevation band using their recorded rate of change with altitude. The daily mean WS from AWS2 were assumed to be independent of altitude, because the WS data on glacier are considered too sparse to derive a general scheme to quantitatively assess the spatial distribution of wind speed (Hock & Holmgren, 2005). The precipitation gradient (P_G) was 0.086% per 100 m, based on data during the ablation season recorded at AWS2 and at Burang meteorological station from October 2013 to September 2018. The gradient for T_a for the ablation season (-0.98°C per 100 m) was same to that for the cold season (October to May), using data from AWS1 and from the two air temperature and humidity probes on the glacier from October 2018 to September 2019. In the same way, the gradient in RH was calculated to be 2.31% per 100 m and 1.52% per 100 m for the ablation season and the cold season, respectively. The S_{in} gradients for the ablation season ($5.4 \text{ W m}^{-2} 100 \text{ m}^{-1}$) and for the cold season ($1.7 \text{ W m}^{-2} 100 \text{ m}^{-1}$) were calculated based on the data recorded at AWS1 and AWS2 from October 2012 to September 2018. The increases in S_{in} with altitude were also found at Guliya Ice Cap (Li et al., 2019). For elevations above the 6,076 m a.s.l. (the elevation of the highest air temperature and humidity probe), we assumed that RH and S_{in} did not change with increasing altitudes.

The densities for fresh snowfall and ice were assumed to be 200 and 900 kg m^{-3} , respectively. For each elevation band at Naimona'nyi Glacier, the temperature at 10 m ice depth was interpolated using the multi-annual mean air temperature recorded at AWS1 and assuming a constant temperature gradient of $-0.005^\circ\text{C m}^{-1}$ through the ice (Yang et al., 2013). The glacier boundary for Naimona'nyi Glacier from the Second Chinese Glacier Inventory (Guo et al., 2015) and the 90 m Shuttle Radar Topography Mission digital elevation model (<https://earthexplorer.usgs.gov/>) was used to derive the glacier area for each elevation band.

In this study, most of the physical parameters used in the EMB model came from measurements and published data. Only the parameters of albedo model were adjusted to achieve the best agreement between the modeled and measured mass balance data (considering both glacier-wide mass balance and the mass balance at stakes) during the 2011–2018 period (from October 2011 to September 2018). Using the area-averaged method stated in Section 2.2.1, the modeled glacier-wide mass balance and energy balance and their components were calculated. There are eight parameters in the albedo parameterization and we focused on adjusting the fresh snow albedo and ice_a (one parameter of the ice albedo parameterization). The mass balance first was calculated using parameters from Yang et al. (2013), however this resulted in an underestimation of the mass loss when compared to measured values. The mass balance calculations were therefore recalculated by changing the assumed values for fresh snow albedo and ice_a to minimize the differences between measured and modeled mass balance data (the glacier-wide mass balance and mass balance at stakes) during the 2011–2018 periods.

3.2. Data Processing

To obtain a continuous data series from October 2010 to September 2018, gaps in the time series of daily mean T_a , RH, and S_{in} from AWS1 between October 2010 and September 2013 were filled using observations from Burang meteorological station, interpolated using the linear regression relationship established between Burang meteorological station data and the available AWS2 data for each month. Gaps in the time series of daily mean WS from AWS2 in October 2010, and between April 2012 and September 2012 were filled following the same method, using WS data from ERA5 and AWS2. This interpolation method has been used in some studies of glacier mass changes on the TP (Yang et al., 2016; Zhu, Yao, Yang, Xu, Wu, Wang, & Xie, 2018). Daily S_{in} at Burang meteorological station was estimated from the recorded sunshine duration, RH, T_a , air pressure, and geographical information (latitude, longitude, and altitude) using the model proposed by Yang et al. (2010). The reconstructed and observed meteorological variables are compared in Figure S3. Gaps in the time series of precipitation from October 2010 to September 2013 were filled with the ERA5 daily precipitation data for the appropriate ERA5 grid cell, using the method proposed by Yang et al. (2013). Cumulative number of precipitation events, cumulative precipitation amount and monthly precipitation were used to justify the reliability of the reconstructed precipitation (Figure S4).

3.3. Uncertainty Analysis

In highly glacierized regions, uncertainty about precipitation is from large spatial variability of precipitation due to orographic effects, snowdrift and wind-induced undercatch in precipitation measurements. The best method to correct undercatch in precipitation depends on subjectivity or local knowledge (Ménard et al., 2019). Using the measured precipitation without correction, our energy and mass balance model could accurately reproduce the observed mass balance at different altitudes and at glacier-wide scale during the 2011–2018 period. In addition, for glaciers in the Himalayas, some studies about the simulated mass balance by the glacier model does not correct precipitation using wind speed (Azam et al., 2014, 2020; Fujita & Nuimura, 2011; Sunako et al., 2019). Thus, we do not correct precipitation using wind speed. We tend to think that the uncertainties about precipitation from orographic effects, snowdrift and wind-induced undercatch were contained in precipitation gradient (P_G). We set the uncertainty for P_G as 10%, which value have been used in some studies (Azam et al., 2020; Ragettli et al., 2013). We performed sensitivity tests to quantify the uncertainty in the modeled annual glacier-wide mass balance by changing the assumed value for one input parameter at a time, leaving all other glacier parameters unchanged. When P_G was changed by 10%, the uncertainty in modeled annual glacier-wide mass balance was 0.003 m w.e. a^{-1} (Table S4). Partitioning snowfall and rainfall from precipitation also caused some uncertainties for precipitation, which linked to two critical air-temperature thresholds for rain (T_{rain}) and snow (T_{snow}), especially for T_{snow} . The minimum T_{snow} was found to be -0.5°C for a maritime glacier (Yang et al., 2013). The T_{snow} and T_{rain} was changed by 0.5°C , the uncertainty in modeled glacier-wide mass balance was 0.015 and 0 m w.e. a^{-1} , respectively (Table S4). These two low uncertainties were due to low T_a which caused almost all the precipitation to fall as snow on Naimona'nyi Glacier.

Some other parameters required by the EMB model were unavailable, including the parameters for the albedo model, and the parameters for the parameterizations of turbulent heat fluxes. Uncertainties associated

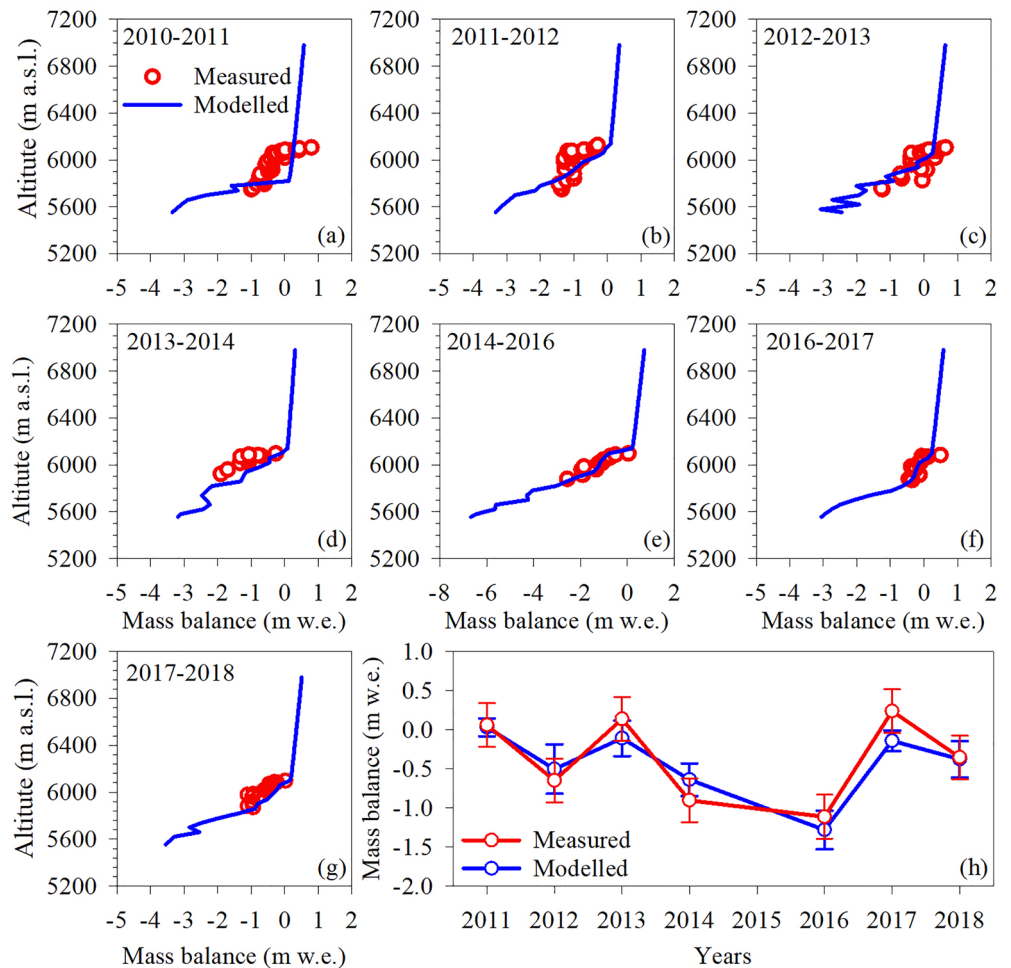


Figure 2. Comparison of modeled (blue line) and measured (red circle) point mass balances at different altitudes in different years (a–g), and modeled and measured glacier-wide mass balance with their uncertainties in different years (h) on Naimona'nyi Glacier. The 2016 in figure h indicated the 2014–2016 period.

with the values assumed for these parameters can greatly influence the model results (Giesen et al., 2008; Hock & Holmgren, 2005; Reijmer & Hock, 2008; Zhu et al., 2015). The uncertainties for parameters in the albedo model and bulk coefficient in turbulent heat fluxes are unknown, and these parameters were changed by $\pm 10\%$ from their original/calibrated values. When parameters in the model are unknown, this is a common method to estimate the parametric uncertainty (Azam et al., 2020; Ragettli et al., 2013). Of all the parameters we tested, highest sensitivity was for fresh snow albedo (a_{snow}) of the albedo model (Table S4). The EMB model was re-run using the modified values for fresh snow albedo in Table S4 to generate a new series of annual glacier-wide mass balance. The difference between new data series and the initial mass balance data series was taken as the uncertainty in the modeled glacier-wide mass balance for each year (Figure 2h). In addition, the uncertainty in glaciological mass balance is due to uncertainties in the point measurements, uncertainties related to the representativeness of the point measurements and the extrapolation method from point measurements to the entire glacier area (Kenzhebaev et al., 2017; Thibert et al., 2008). We adopt an average uncertainty of $\pm 0.28 \text{ m w.e. a}^{-1}$ for the measured annual glacier-wide mass balance calculated using the profile method, as found by Kenzhebaev et al. (2017).

4. Results

4.1. Observed Mass Balance and Model Validation

The point mass balance observed at stakes on Naimona'nyi Glacier shows that mass balance increases gradually with altitude and there are large annual variations, even at the same altitude (Figure 2). The point mass balance measured at locations below 6,070 m a.s.l. was almost always negative during the 2011–2018 period. A negative mass balance was also found in 2012/13 at the higher elevation of 6,125 m a.s.l., with a value of -0.29 m w.e. (Figure 2c). The vertical gradient for the annual mass balance ranged from 0.22 m w.e. per 100 m in 2011/12 to 0.65 m w.e. per 100 m in 2013/14, with a mean of 0.39 m w.e. per 100 m. Modeled and measured annual mass balance at different altitudes are shown in Figure 2. Earlier studies have found that complicated topography and snowdrift may lead to high spatial variability for precipitation and for its gradient across the glacier surface, particularly in the accumulation zone (Zhang et al., 2012; Zhao et al., 2016). These can introduce the spatial heterogeneity of mass balance at the same altitude by changing albedo, melt energy and accumulation, which explains the mismatches between the measured and modeled mass balance at some locations on the glacier (Figure 2). The RMSE between the measured and simulated mass balances at all the stakes was 0.47 m w.e. a^{-1} for eight years during the 2011–2018 period, which is similar to the value in Zhao et al. (2016) and Zhang et al. (2018). This is interpreted as showing that the observed and modeled mass balance at stakes generally agree. In addition, the modeled mass balance above $\sim 6,100$ m a.s.l. increased slowly with increasing altitudes, and the modeled mass balance below $\sim 6,100$ m a.s.l. generally increased strongly with decreasing elevations (Figure 2). This is because the mass balance above $\sim 6,100$ m a.s.l. was determined by snowfall and sublimation, and the mass balance below $\sim 6,100$ m a.s.l. was controlled by melt, as suggested by Zhu et al. (2020).

The measured annual glacier-wide mass balance has strong interannual variability, ranging from -0.9 m w.e. a^{-1} in 2013/14 to 0.23 m w.e. a^{-1} in 2016/17 (Figure 2h), with a mean value of -0.32 m w.e. a^{-1} over the observed period. Figure 2h shows that there is good agreement between the modeled and measured annual glacier-wide mass balances, with a correlation coefficient of 0.94 and an RMSE of 0.2 m w. e. a^{-1} . The largest underestimation of modeled annual glacier-wide mass balance occurred in 2016/17 and was probably related to model underestimation of accumulation above 6,075 m a.s.l. (Figure 2f). If we exclude the annual glacier-wide mass balance in 2016/17, the measured and modeled annual glacier-wide mass balance agree reasonably well, with a mean bias error of -0.01 m w.e. a^{-1} and an RMSE of 0.17 m w.e. a^{-1} . This agreement demonstrates that the calibrated EMB model can be used to evaluate changes in mass balance and their relationship of these to climate drivers.

4.2. Meteorological Observations on Naimona'nyi Glacier

The daily mean T_a fluctuated between -24.3 and 7.4°C , with a mean of -6.0°C (Figure 3a and Table 1). The seasonal T_a varied from a low of -15.9°C in January to a high of 3.8°C in July (Figure 3b). The daily mean RH changed from 3% to 99% (Figure 3c). The highest mean monthly RH was in July and August, and the lowest value was observed in December (Figure 3d). The daily mean WS reached values up to 15 m s^{-1} between December and February, and was always less than 6 m s^{-1} between June and August (Figure 3e). In the cold season, the frequency for daily precipitation was low and there were some extreme precipitation events (Figure 3g). The annual monthly precipitation cycle has a strong peak in July and August, and a secondary peak between January and March (Figure 3h). The mean monthly precipitation was lowest in November and December. The mean annual total precipitation was 292.5 mm, and 70% of annual total precipitation occurred during the ablation season, indicating that Naimona'nyi Glacier is a summer-accumulation type glacier (Sakai et al., 2015). On an interannual scale, precipitation was strongly correlated with RH, with correlation coefficients of 0.84 ($p < 0.05$) and 0.92 ($p < 0.01$) in the cold and ablation seasons, respectively. The daily mean S_{in} fluctuates significantly due to the influence of cloudiness (Figure 3i). The monthly mean S_{in} was greatest in April, May, and June and smallest in December and January (Figure 3j), with a mean of 226 W m^{-2} .

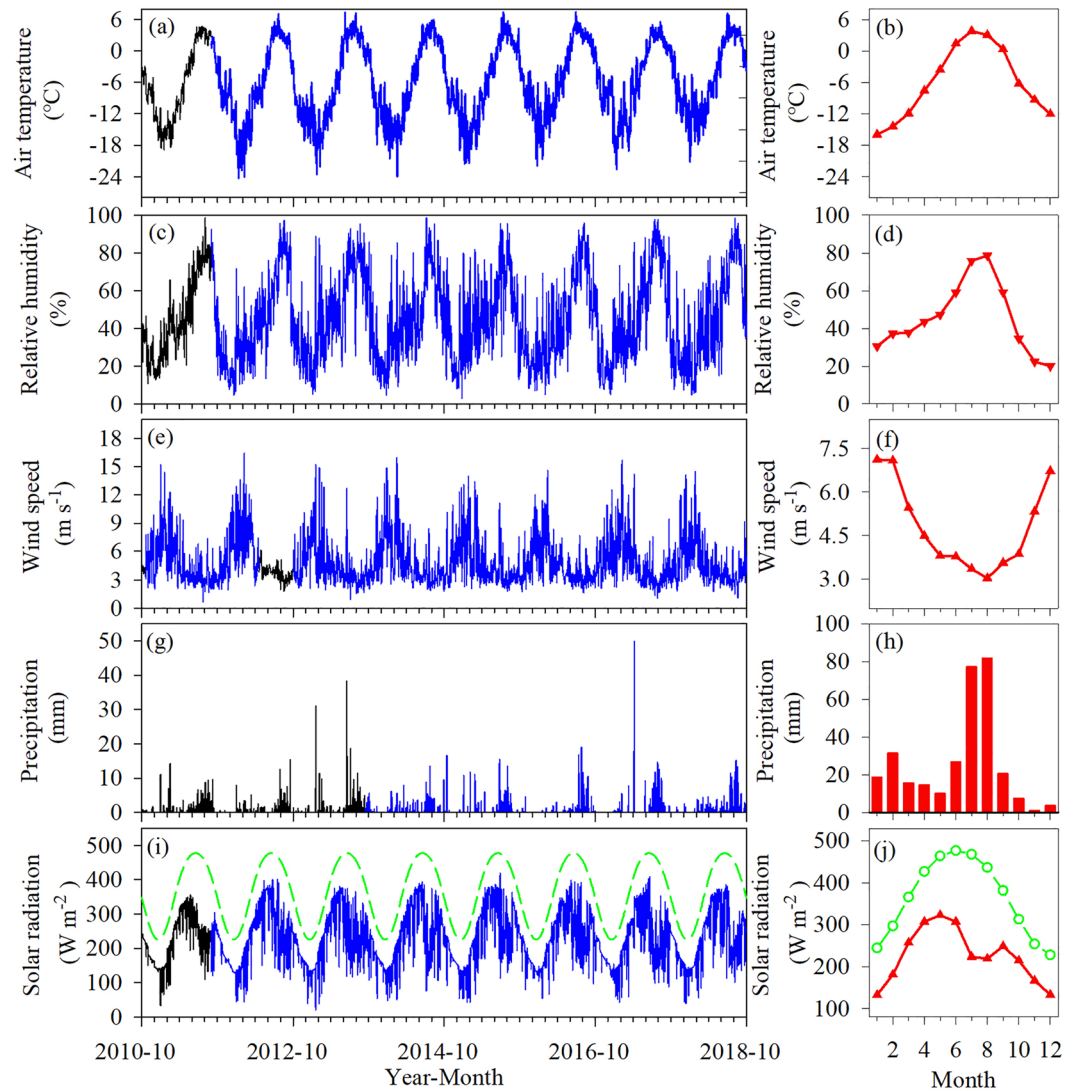


Figure 3. Daily values of (a) air temperature, (c) relative humidity, and (i) incoming shortwave radiation at AWS1 site, and (e) wind speed and (g) precipitation at AWS2 site. Blue lines denote measurements from the AWSs and black lines indicate the corrected values. Dashed line in Figure 3i indicates the calculated daily mean solar radiation at the top of the atmosphere. The mean monthly values of (b) 2 m air temperature, (d) relative humidity, and (j) incoming shortwave radiation at AWS1 site, and (f) wind speed, and (h) precipitation at AWS2 site. Dashed line in Figure 3j indicates the calculated mean monthly solar radiation at the top of the atmosphere. AWS, automatic weather stations.

4.3. Seasonal and Interannual Changes in Individual Components of the Glacier-Wide Energy Balance

Net shortwave radiation (S_{net}) is the largest contribution to incoming energy and varied greatly through the year, with higher values in the ablation season than in the cold season (Figure 4a). The average monthly S_{net} was minimum in January and December and maximum in June. Net longwave radiation (L_{net}) was the largest energy sink throughout the year and was less seasonally variable than S_{net} (Figure 4a). The mean monthly L_{net} was smallest between April and June and highest in July and August. H_{sen} was positive for most of the year and slightly negative for some days in the ablation season, particularly in June (Figure 4a). In contrast, H_{lat} was negative for most of the year, but was positive for some days in the ablation season, for example for some days in August. Q_G was a minor energy source and the mean monthly Q_G varied from -5 W m^{-2} in May to 8 W m^{-2} in December. Surface melt mainly occurred from June to September and the largest mean monthly Q_M was in June and July.

Table 1
Seasonal Mean Values of Meteorological Variables at the AWS Sites and of Glacier-Wide Mass Balance Components and Energy Balance Components

	Variables	Ablation season	Cold season	Annual
AWSs	T_a (°C)	2.2	−10	−5.9
	RH (%)	68.1	33.7	45.1
	WS (m s ^{−1})	3.4	5.5	4.8
	P (mm)	205.6	86.9	292.5
	S_{in} (W m ^{−2})	250	214	226
Glacier-wide	Snowfall (m w.e.)	0.21	0.09	0.3
	Refreezing (m w.e.)	0.06	0	0.06
	Sublimation (m w.e.)	−0.04	−0.14	−0.18
	Melt (m w.e.)	−0.56	0	−0.56
	Mass balance (m w.e.)	−0.33	−0.05	−0.38
	Rain (m w.e.)	0.03	0	0.03
	S_{in} (W m ^{−2})	274	222	240
	Albedo	0.66	0.69	0.68
	S_{out} (W m ^{−2})	−182	−153	−163
	S_{net} (W m ^{−2})	92	69	77
	L_{in} (W m ^{−2})	233	174	194
	L_{out} (W m ^{−2})	−300	−245	−263
	L_{net} (W m ^{−2})	−67	−71	−69
	R_{net} (W m ^{−2})	25	−2	8
	H_{sen} (W m ^{−2})	3	17	12
	H_{lat} (W m ^{−2})	−11	−18	−16
	Q_G (W m ^{−2})	1	3	2
Q_M (W m ^{−2})	18	0	6	

AWSs, automatic weather stations.

We analyzed interannual changes in the individual components of energy balance for different seasons (Figure 5a) and found the standard deviation for all components to be significantly greater in the ablation season than in the cold season. For the ablation season, the standard deviations for S_{out} and S_{in} were significantly larger than those for the other energy balance components and the standard deviation for H_{lat} was slightly lower than that for Q_M , S_{out} , S_{in} , and H_{lat} may play an important role in dominating the variations in melt energy. We further assessed the relationship between Q_M and S_{in} , S_{out} , albedo, and H_{lat} in the ablation season to determine the main driver for the interannual variability in Q_M . The correlations between S_{in} and Q_M ($r = 0.46$, $p = 0.46$) and between H_{lat} and Q_M ($r = -0.55$, $p = 0.15$) were not significant, while the correlations between S_{out} and Q_M , and between albedo and Q_M were -0.8 ($p < 0.05$) and -0.86 ($p < 0.01$), respectively. We therefore conclude that variations in albedo during the ablation season, which are linked to S_{out} , controlled the interannual variability of melt energy on Naimona'nyi Glacier.

4.4. Seasonal and Interannual Changes in Individual Components of the Glacier-Wide Mass Balance

Surface melt was the largest component of the annual mass balance, with a mean annual value of -0.56 m w.e. a^{−1} (Table 1). Surface melt primarily occurred in the ablation season and most (76%) surface melt was in June and July (Figure 4b). The dominant source of mass gain was snowfall; the mean annual snowfall was 0.3 m w.e. a^{−1}. Almost all precipitation fell on glacier surface as snow because of Naimona'nyi Glacier's high elevation and associated low T_a . Around 70% of the total annual snowfall occurred during the ablation season, and about 52% of the total annual snowfall fell in July and August (Figure 4b). Snowfall in the ablation season was 0.12 m w.e. a^{−1} higher than in the cold season (Table 1). Sublimation/evaporation was the third largest contributing term in the annual mass balance and occurred in both ablation and cold seasons, and it was the largest mass loss in the cold season (Table 1). Refreezing was the smallest contributor to the annual mass balance and occurred only in the ablation season, especially for June and August.

The average annual cycle shows there was significant mass loss in June and July due to strong melt, which was significantly greater than the gains made from snowfall. A slight negative mass balance in the other months is the result of limited snowfall, which is too little to compensate for the mass loss through sublimation in the cold season and through melt in August and September (Figure 4b). The mass balance was very close to zero during the cold season, while surface melt and snowfall during the ablation season dominated the annual mass balance.

To analyze interannual changes in the components of the mass balance on Naimona'nyi Glacier, the standard deviations was calculated for the individual components of the mass balance for the different seasons (Figure 5b). Interannual variability in the mass balance for the cold season was driven by interannual variability in snowfall and sublimation, and was very low. The magnitude of the interannual variations in melt was significantly greater than the variability for other component of the mass balance both during the ablation season, and when the whole year was considered. Snowfall had the second highest interannual variability. We can therefore conclude that interannual variations in the mass balance were mainly driven by the interannual variability in melt during the ablation season, and that variability in the annual snowfall also influenced interannual variability in the mass balance.

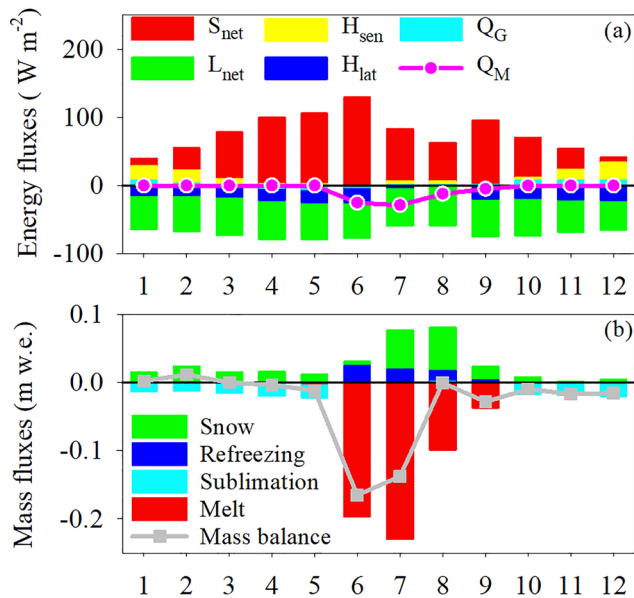


Figure 4. Average monthly energy balance components (a) and mass balance components (b) during the 2011–2018 period.

4.5. Mass Balance Sensitivity

It is important to assess mass balance sensitivities so that we can understand glacier mass balance response to climate change. The sensitivity of the mass balance for Naimona'nyi Glacier was calculated by re-running the EMB model with uniform perturbation applied to air temperature (or precipitation), while keeping precipitation (or air temperature) and other variables remained unchanged (Oerlemans et al., 1998). The sensitivity of mass balance to air temperature perturbation was $0.37 m w.e. a^{-1} °C^{-1}$, and to precipitation perturbation was $0.1 m w.e. a^{-1} (10\%)^{-1}$, which are similar to the sensitivities reported for Stok Glacier in the western Himalayas ($0.32 m w.e. a^{-1} °C^{-1}$ and $0.12 m w.e. a^{-1} (10\%)^{-1}$, Soheb et al., 2020).

To find climate conditions corresponding to a net zero mass balance, the EMB model was run iteratively, with only precipitation (or air temperature) changed until the average annual glacier-wide mass balance during the 2011–2018 period was zero. The results show that zero mass balance may be achieved if either the current average annual air temperature reduces by $1.1°C$ or annual precipitation increases by 49%. Present climate conditions are too warm and/or dry which caused Naimona'nyi Glacier in a mass deficit state. The standard deviations for T_a during ablation season ($0.46°C$) and for the annual total precipitation (22%) was lower than $1.1°C$ and 49%, respectively, showing that there is little possibility of a climate shift great enough to stall the state of mass loss for Naimona'nyi Glacier.

5. Discussion

5.1. Climate Factors Driving Interannual Variability in the Mass Balance for Naimona'nyi Glacier

To explore the influence of key climate variables on mass balance fluctuations for Naimona'nyi Glacier, we examined relationships between the annual glacier-wide mass balance and local meteorological factors (T_a and precipitation) (Figure 6). The annual mass balance is weakly correlated with ablation-season T_a (Figure 6a), which is related to L_{in} , turbulent heat fluxes, and snowfall due to its influence on the ratio of snowfall to precipitation (Oerlemans, 2001; Zhu, Yao, Yang, Xu, Wu, & Wang, 2018). However, as shown in Section 4.3, interannual variability in Q_M during the ablation season was driven by interannual changes in albedo for the ablation season, not by ablation-season L_{in} , H_{sen} or H_{lat} . In addition, there was no significant correlation between T_a and snowfall ($r = 0.11, p = 0.79$) or albedo ($r = -0.36, p = 0.38$) for the ablation season. This is why the correlation between the annual mass balance and ablation-season T_a is weak. Instead, the annual mass balance was strongly correlated with annual precipitation (Figure 6b). In addition, following the method proposed by Zhu et al. (2020), we compared the mass balance sensitivity to a temperature perturbation of $\pm 0.31 K$ (one standard deviation of ablation-season T_a) with its sensitivity to a precipitation perturbation of $\pm 22\%$ (one standard deviation of annual precipitation). The sensitivity of the mass balance to changes in annual precipitation was found to be $0.22 m w.e. a^{-1}$, which is higher than the sensitivity to changes in air temperature, which was $0.11 m w.e. a^{-1}$. We therefore conclude that changes in annual precipitation drove interannual variability in the annual mass balance for Naimona'nyi Glacier.

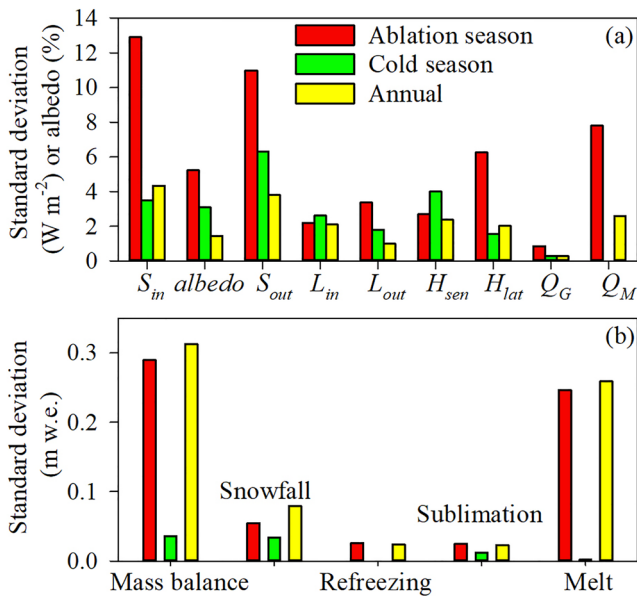


Figure 5. The standard deviations of glacier-wide energy balance components (a) and mass balance components (b) in different seasons during the 2011–2018 period.

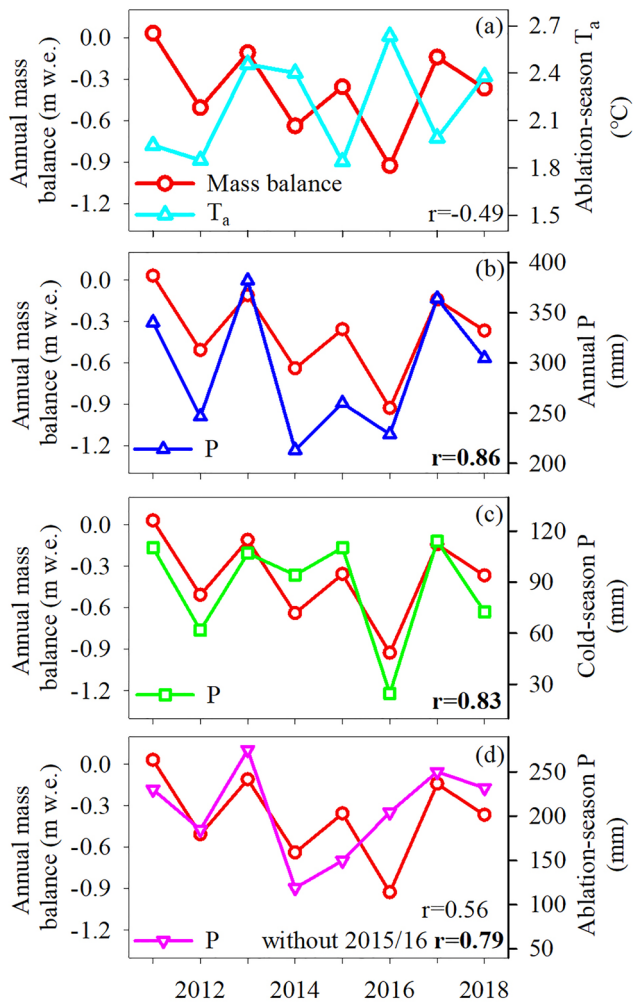


Figure 6. The correlations of annual glacier-wide mass balance versus ablation-season air temperature (a), annual precipitation (b), cold-season precipitation (c) and ablation-season precipitation (d) during the 2011–2018 period. The bold black font indicated that the p was less than 0.05.

We analyzed how seasonal precipitation affected the changes in the annual mass balance. Changes in L_{in} , turbulent heat fluxes and the ratio of snowfall to precipitation are small between 2010/11 and 2017/18, suggesting that slightly higher T_a during the ablation season may not have been the primary driver for the increased mass loss in 2017/18 (relative to 2010/11) (Table S5). Lower precipitation during the cold season in 2017/18 led to lower albedo, higher Q_M and lower mass balance for June and July, contributing to higher ablation-season Q_M and lower annual mass balance in 2017/18, relative to 2010/11 (Tables S5 and S6). In addition, strong relationships were found between cold-season precipitation and June–July albedo (Figure 7a), between cold-season precipitation and ablation-season Q_M ($r = 0.85$, $p < 0.05$) and between cold-season precipitation and annual mass balance (Figure 6c). These relationships suggest that interannual variability in the mass balance is likely to be accounted for by precipitation during the cold season, which drove a change in albedo for June and July and a change in melt energy in the ablation season.

Precipitation during the ablation season impacts surface melt by impacting on albedo and snow accumulation, which then affects the changes in the annual mass balance (Zhu, Yao, Yang, Xu, Wu, Wang, & Xie, 2018). Precipitation in the cold season, and T_a for the ablation season, were similar in 2012/13 and 2013/14 (Table S5). Lower precipitation during the ablation season in 2013/14 led to lower snow accumulation, lower albedo and higher Q_M in the ablation season, especially for latter two factors, relative to 2012/13. This resulted in lower annual mass balance for 2013/14 than for 2012/13. Precipitation during the cold season was lowest and T_a for the ablation season was highest in 2015/16 (Figure 6). This reduced the relative influence of ablation-season precipitation on albedo and Q_M in the ablation season, and resulted in the lowest annual mass balance. With the exception of 2015/16, correlations between ablation-season precipitation and ablation-season albedo (Figure 7b), between ablation-season precipitation and ablation-season Q_M ($r = 0.67$, $p = 0.1$), and between ablation-season precipitation and annual mass balance are significant (Figure 6d). This shows that by altering the melt energy and albedo in the ablation season, and partly by impacting snow accumulation in the ablation season, ablation-season precipitation was another important factor influencing the interannual variability in the mass balance. In addition, another sensitivity test was carried out to assess whether ablation-season precipitation or cold-season precipitation was more important for influencing interannual variability in the mass balance. In this test, we modified precipitation during the ablation season by +52.4 mm (one standard deviation of the ablation-season precipitation during the 2011–2018 period) and left all other variables unchanged, resulting in a mass balance sensitivity of 0.13 m w.e. a^{-1} . We then changed precipitation over the cold season by +52.4 mm (the same perturbation amount for the ablation season) and left all other variables unchanged, which resulted in a mass balance sensitivity of 0.15 m w.e. a^{-1} . These results may show that precipitation during the ablation season and during the cold season had an almost equal influence on changes in the annual mass balance. In addition, such sensitivity analysis also shows that changes in cold-season precipitation mainly influenced June–July mass balance and changes in ablation-season precipitation mainly influenced ablation mass balance (Figure S5). In summary, interannual variability in the mass balance for Naimona'nyi Glacier is mainly accounted for by changes in annual precipitation, which mainly changed albedo and melt energy during the ablation season.

modified precipitation during the ablation season by +52.4 mm (one standard deviation of the ablation-season precipitation during the 2011–2018 period) and left all other variables unchanged, resulting in a mass balance sensitivity of 0.13 m w.e. a^{-1} . We then changed precipitation over the cold season by +52.4 mm (the same perturbation amount for the ablation season) and left all other variables unchanged, which resulted in a mass balance sensitivity of 0.15 m w.e. a^{-1} . These results may show that precipitation during the ablation season and during the cold season had an almost equal influence on changes in the annual mass balance. In addition, such sensitivity analysis also shows that changes in cold-season precipitation mainly influenced June–July mass balance and changes in ablation-season precipitation mainly influenced ablation mass balance (Figure S5). In summary, interannual variability in the mass balance for Naimona'nyi Glacier is mainly accounted for by changes in annual precipitation, which mainly changed albedo and melt energy during the ablation season.

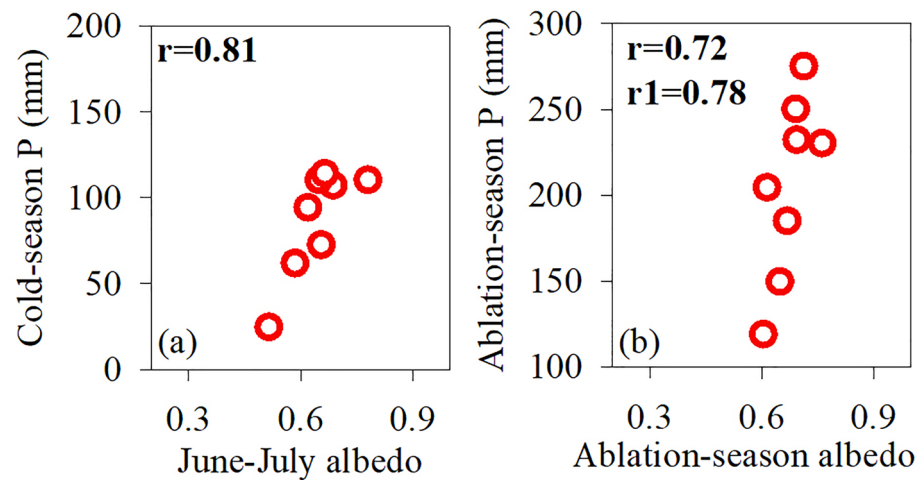


Figure 7. The correlations between cold-season precipitation and June-July albedo (a), and between ablation-season precipitation and ablation-season albedo (b). The bold black font indicated that the p was less than 0.05; r is the correlation coefficient for eight years during the 2011–2018 period and $r1$ is the correlation coefficient for seven years during the 2011–2018 period without 2015/16.

5.2. Different Variations in the Mass Balance for Tibetan Glaciers Over the Past Two Decades and Possible Relationship With Atmospheric Circulation

According to the annual mass balance fluctuations, two periods could be roughly identified (Figure S6). For Naimona'nyi and Chhota Shigri glaciers, the annual mass balance was always lower than -0.4 m w.e. a^{-1} during the 2000–2009 period (October 1999 to September 2009), while it was higher than -0.4 m w.e. a^{-1} during the 2010–2019 period (October 2009 to September 2019) with several positive values. In addition, if we get rid of the most negative mass balance in 2006/07 and the most positive mass balance in 2016/17, the mean mass balance on Naimona'nyi Glacier was 0.15 m w.e. a^{-1} higher during the 2010–2018 period than during the 2000–2009 period. For Chhota Shigri Glacier, if the most negative mass balance in 2002/03 and the most positive mass balance in 2018/19 were deleted, the mean mass balance was 0.39 m w.e. a^{-1} higher during the 2010–2019 period than during the 2000–2009 period. It seems that the differences of mass balance between two periods on both glaciers were stable.

Although, there were differences in the length of time series of mass balance for different glaciers during the 2000–2019 period, only two periods (the 2000–2009 period and the 2010–2019 period) are defined to compare interdecadal changes in the mass balance for glaciers on different parts of the TP and in the surrounding areas to understand the drivers for glacier behaviors in these regions. Figure 8 shows the average mass balances for eight glaciers on the TP and in the surrounding areas during the 2000–2009 period and during the 2010–2019 period, and the differences between them. Mass balance data were not available for every year during the 2000–2019 period for all eight glaciers, however differences in the mean mass balance, calculated for the 2000–2009 period and for the 2010–2019 period, should not be significantly affected. For example, in-situ measurements show that the mean mass balance for Chhota Shigri Glacier was 0.62 m w.e. a^{-1} higher during the 2010–2019 period than during the 2003–2009 period. If the modeled annual mass balances for 1999/2000 to 2001/02 from Azam et al. (2014) are appended to the 2002/03 to 2008/09 data series, then the difference between the two periods changes to 0.43 m w.e. a^{-1} , which is very close to the difference found using the incomplete data series.

Zhadang Glacier in the south TP, Xiaodongkemadi Glacier in the central TP, Qiyi Glacier in the northeast TP, Urumqi Glacier No.1 in the east Tien Shan and Ts. Tuyuksuyskiy Glacier in the inner Tien Shan experienced greater mass loss during the 2010–2019 period than during the 2000–2009 period (Figure 8a). The interdecadal changes in glacier mass balance were associated with changes in local ablation-season T_a and/or local seasonal precipitation (Azam et al., 2014; Vincent et al., 2013; Yang et al., 2016; Zhang et al., 2012; Zhu, Yao, Yang, Xu, Wu, Wang, & Xie, 2018). We looked the difference between the mean ERA5 values during the 2010–2019 period and those during the 2000–2009 period for ablation-season T_a , cold-season precipitation

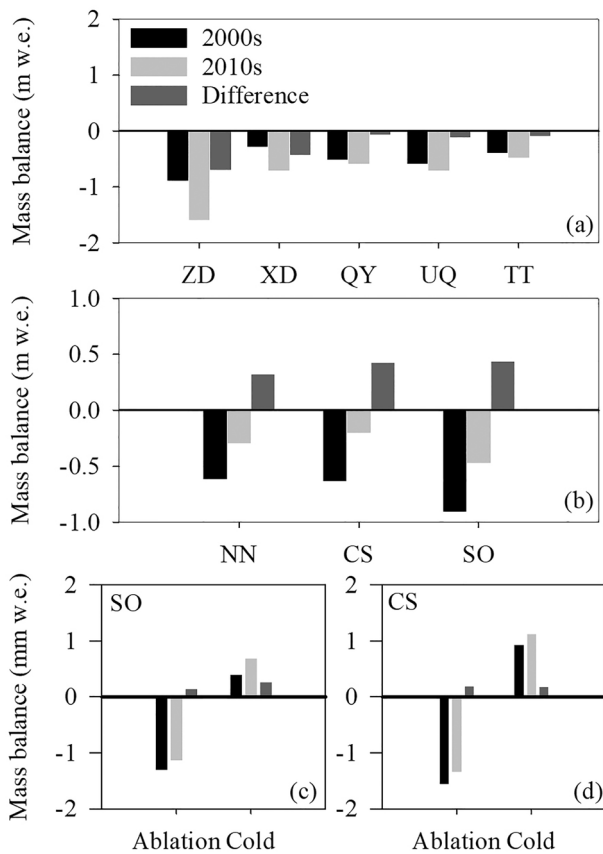


Figure 8. (a) The mean mass balances during the periods of 2000–2009 and 2010–2019, and the difference between the two periods for five glaciers on the TP and in the surrounding areas. 2000s: During the 2000–2009 period; 2010s: During the 2010–2019 period; ZD is Zhadang Glacier. Its time series of annual mass balance during the 2006–2016 period are from Yao et al. (2018); XD is Xiaodongkemadi Glacier. Its time series of annual mass balance during the 2000–2017 period are from Yao et al. (2019); UQ and TT are Urumqi No. 1 and Ts. Tuyuksuyskiy glaciers, respectively. Their time series of annual mass balance during the 2000–2019 period are from WGMS (2020); (b) the mean mass balances during the periods of 2000–2009 and 2010–2019, and the difference between the two periods for three glaciers in the western Himalayas. NN is Naimona'nyi Glacier. Its time series of annual mass balance were modeled by Zhao et al. (2016) during the 2000–2004 period and in 2006/07, and measured in the other years during the 2000–2018 period; CS is Chhota Shigri Glacier. Its time series of annual mass balance were modeled by Azam et al. (2014) during the 2000–2002 period, and measured by Mandal et al. (2020) during the 2003–2019 period; SO is Stok Glacier. Its time series of annual mass balance were modeled by Mandal et al. (2020) during the 1999–2019 period; (c) the averaged seasonal mass balances during the periods of 1999–2009 and 2012–2019, and the difference between these periods for Stok Glacier. Its time series of seasonal mass balances were modeled by Soheb et al. (2020) during the 1999–2019 period; (d) the magnitude of seasonal mass balances during the periods of 2000–2009 and 2010–2019, and the difference between these periods for Chhota Shigri Glacier. Its time series of seasonal mass balances were modeled by Azam et al. (2014) during the 2000–2009 period and measured during the 2010–2019 period by Mandal et al. (2020). (Difference: 2010–2019 minus 2000–2009).

and ablation-season precipitation. Over most of the TP and surrounding areas, T_a in the ablation season was higher during the 2010–2019 period than during the 2000–2009 period, and the increase was strongest on the western and southern parts of the TP (Figure 9a). Precipitation during the ablation season has reduced over the last 20 years on the central TP and in the inner Tien Shan (Figure 9b). Zhadang, Xiaodongkemadi, Qiyi, Urumqi No.1, and Ts. Tuyuksuyskiy glaciers were summer-accumulation type glaciers (Maussion et al., 2014; Sakai et al., 2015) and more sensitive to ablation-season T_a than to annual precipitation (Liu & Liu, 2016; Yao et al., 2019; Zhu, Yao, Yang, Xu, Wu, & Wang, 2018). The mass balance for these five glaciers therefore has an accelerating negative trend over the past two decades that is mainly attributable to the increasing ablation-season T_a . Xiaodongkemadi and Zhadang glaciers have experienced greater mass loss than the other three glaciers over the last 20 years due to a greater rise in ablation-season T_a and a reduction in ablation-season precipitation. The meteorological stations near these glaciers have recorded similar climate trends to those in the ERA5 data (Table S2).

The mean annual mass balance for three glaciers in the western Himalayas was less negative during the 2010–2019 period than during the 2000–2009 period (Figure 8b) and we looked for an explanation for this. For Naimona'nyi Glacier (summer-accumulation type glacier), we can speculate that higher annual precipitation led to a higher mean annual mass balance during the 2010–2019 period, relative to the 2000–2009 period, by reducing the ablation-season Q_M and increasing the accumulated snowfall. These suggestions are based on our analysis in Section 5.1, ERA5 data and observations from Burang meteorological station (Figure 9 and Table S2). For Stok and Chhota Shigri glaciers (winter-accumulation type glaciers), the higher mean annual mass balance during the 2010–2019 period, relative to that during the 2000–2009 period, can be explained by higher cold-season mass balance, resulting from higher cold-season precipitation, and by higher ablation-season mass balance (Figure 8), attributable to both a lower ablation-season T_a and increased ablation-season precipitation during the 2010–2019 period, relative to the 2000–2009 period (Azam et al., 2014; Soheb et al., 2020). Figure 8 shows that at least a half of increased mass balance during the 2000–2019 period are from increased cold-season precipitation. And compared to ablation-season precipitation, cold-season precipitation and ablation-season T_a may be more important drivers for interdecadal variability in the mass balance for Stok and Chhota Shigri glaciers (Azam et al., 2014; Soheb et al., 2020). Given the current knowledge on the relationships between the mass balance and local T_a and local precipitation for three glaciers in the western Himalayas on the interdecadal scales, we now explore if these relationships are widespread across the western Himalayas.

Figure 9a shows that the mean ablation-season T_a for most regions (winter-accumulation type glaciers) of the western Himalayas was lower during the 2010–2019 period than during the 2000–2009 period, while the mean ablation-season T_a for the east part of the western Himalayas (summer-accumulation type glaciers) was slightly higher during the 2010–2019 period than during the 2000–2009 period. Mean precipitation was higher during the 2010–2019 period than during the 2000–2009 period in both the ablation season and the cold season over the western Himalayas (Figures 9b and 9c). These T_a and precipitation anomaly distributions from the ERA5 data over the two periods agree with the temporal distributions

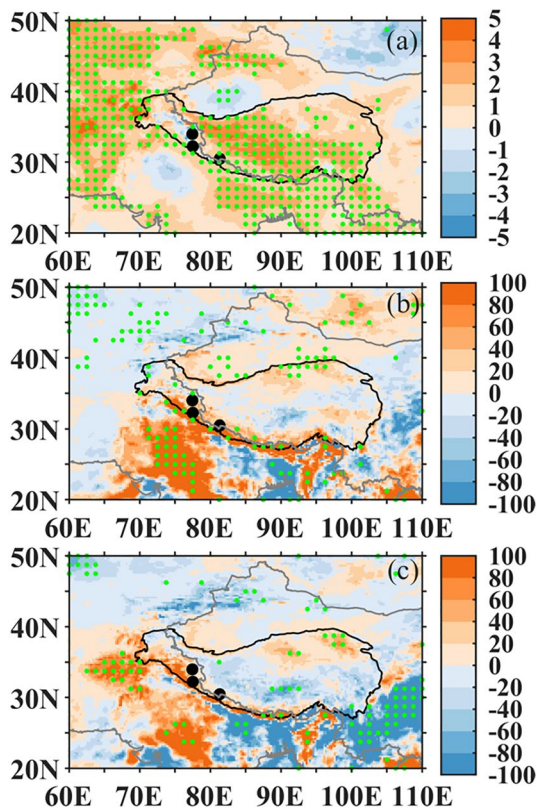


Figure 9. Differences in ablation-season air temperature (a), ablation-season precipitation (b) and cold-season precipitation (c) between the periods of 2000–2009 and 2010–2019. The three black points from south to north indicate the locations of Naimona'nyi, Chhota Shigri and Stok glaciers, respectively. The air temperature and precipitation fields were from ERA5 (Difference: 2010–2019 minus 2000–2009). The dotted areas (green dots) indicated differences that are significant at the 0.1 level.

from measured meteorological data near Naimona'nyi and Stok glaciers (Figure 8 and Table S2). Thus, a higher mean mass balance during the 2010–2019 period than during the 2000–2009 period may be widespread among glaciers in the western Himalayas, and may be partly explained by changes in annual precipitation. Although the ablation-season T_a are important drivers for decadal variability in the mass balance for glaciers in the west part of western Himalayas, we do not discuss the relationship between air temperature and atmospheric circulation. In this work, we focused on how atmospheric circulation affect the glacier mass changes in the western Himalayas through changes in annual precipitation.

Precipitation in the western Himalayas is influenced by the mid-latitude westerlies during the winter and spring, and by the Indian summer monsoon in the summer (Bookhagen & Burbank, 2010; Yao et al., 2013; Yadav et al., 2009). Here we discuss the possible influence of large-scale circulation on cold-season and ablation-season precipitation to consider whether macroscale atmospheric circulation may be a partial driver for the glacier mass changes in the western Himalayas that are discussed above. Geopotential height and wind fields at the 500 hPa level are routinely used to discern the influence of atmospheric circulation on regional climate on the TP (Yang et al., 2016; Liu et al., 2020). We analyzed differences in averaged cold-season geopotential height and wind fields at 500 hPa between the 2000–2009 period and the 2010–2019 period (Figure 10). Figure 10 shows that anomalous anticyclonic circulations occur over Europe, eastern Russia and the Philippines, while anomalous cyclonic circulations exist over North Atlantic, the northwestern Indian Peninsula, and Central Asia. The southerly wind anomalies downstream of the cyclonic anomaly near the northwestern Indian Peninsula cover the most of the Indian Peninsula and northern Arabian Sea. These increased southerly winds effectively increased moisture transport from the Indian Peninsula and northern Arabian Sea to the western Himalayas in the cold season (Figure 10). These circulation patterns for intensifying moisture transporting to the western Himalayas in the winter were also found in Qiu et al. (2019) and Liu et al. (2020). On reaching the high altitude terrain of the western Himalayas, the increase in transported moisture re-

sulted in increased cold-season precipitation during the 2010–2019 period, relative to the 2000–2009 period. The strengthened westerly winds appeared over the North Atlantic (45°N–70°N, 110°W–20°E) and north Asia (Figure 10). Yadav et al. (2009) thought that such circulations maybe correspond to the positive phase of North Atlantic Oscillation (NAO). The mean NAO in the cold season was higher during the 2010–2019 period (without 2009/10) than that during the 2000–2009 period (Figure S7). The mean value of cold-season NAO during the 2010–2019 period was calculated without 2009/10, because cold-season NAO in 2009/10 was extremely low. The higher NAO increases the pressure gradient between subtropical and polar North Atlantic, which intensifies the jet from tropical North Atlantic to Middle East (Yadav et al., 2009). Such intensified Asian jet and the cascading down of Rossby waves from North Atlantic developed low pressure (cyclonic circulation) over south of Caspian Sea (Yadav et al., 2009). Figure 10 shows the similar wind fields that the strengthened westerly winds occurred from tropical North Atlantic to Middle East, the anticyclonic anomaly appeared over Europe and the cyclonic anomaly emerge over the northwestern Indian Peninsula. Such wind fields were also found in Liu et al. (2020). In addition, the jet intensifies the western disturbances (WDs) and produces more precipitation over the northwest India (Yadav et al., 2009). Thus, it is possible that the enhanced NAO caused anomalous cyclone in the northwestern Indian Peninsula and the strengthened western disturbances, which led to higher cold-season precipitation and cold-season mass balance in the western Himalayas during the 2010–2019 period, relative to the 2000–2009 period.

In addition, higher precipitation during the ablation season also contributed to higher mass balance for glaciers in the western Himalayas (especially for its east part) during the 2010–2019 period, relative to the

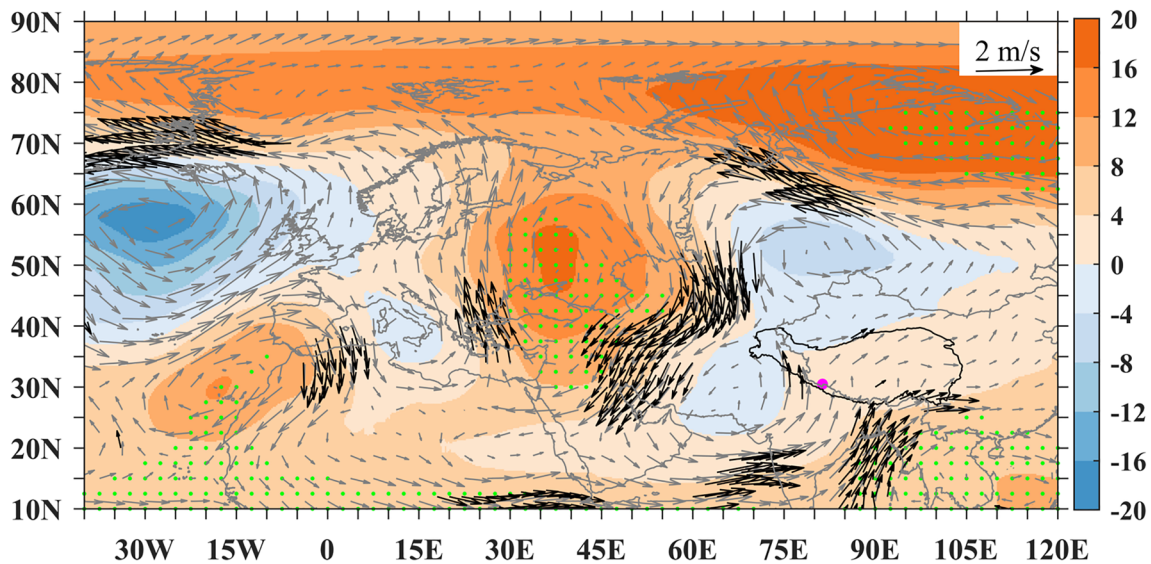


Figure 10. Differences in the mean 500 hPa geopotential heights (gpm) and wind speed field between the periods of 2000–2009 and 2010–2019 during the cold season; the pink point indicates the location of Naimona'nyi Glacier; the 500 hPa geopotential heights and wind speed fields were from the ERA5 (Difference: 2010–2019 minus 2000–2009). The dotted areas (green dots) and black arrows indicated differences that are significant at the 0.1 level.

2000–2009 period. This precipitation change is associated with a 500 hPa cyclonic anomaly over central India that generated southerly and southwesterly flow anomalies to its east (Figure 11). The increased southwesterly flow transported more moisture from the Indian Ocean and central eastern India to the western Himalayas and southwest TP. Dong et al. (2016) thought that such atmospheric circulation pattern indicated the enhanced convection over the central eastern Indian subcontinent, which can transport midtropospheric water vapor from the Indian Ocean and central eastern India to the western Himalayas and the southwest TP through “up-and-over” transport process. The cyclonic anomaly we find here may therefore be controlled by deep convection over the Indian subcontinent (Dong et al., 2016). Sun et al. (2020) thought that the Atlantic multidecadal oscillation (AMO) warm phase induces a wave train of cyclonic and anticyclonic anomalies in summer over Eurasia, and the cyclonic anomalies in the west of the TP in this wave

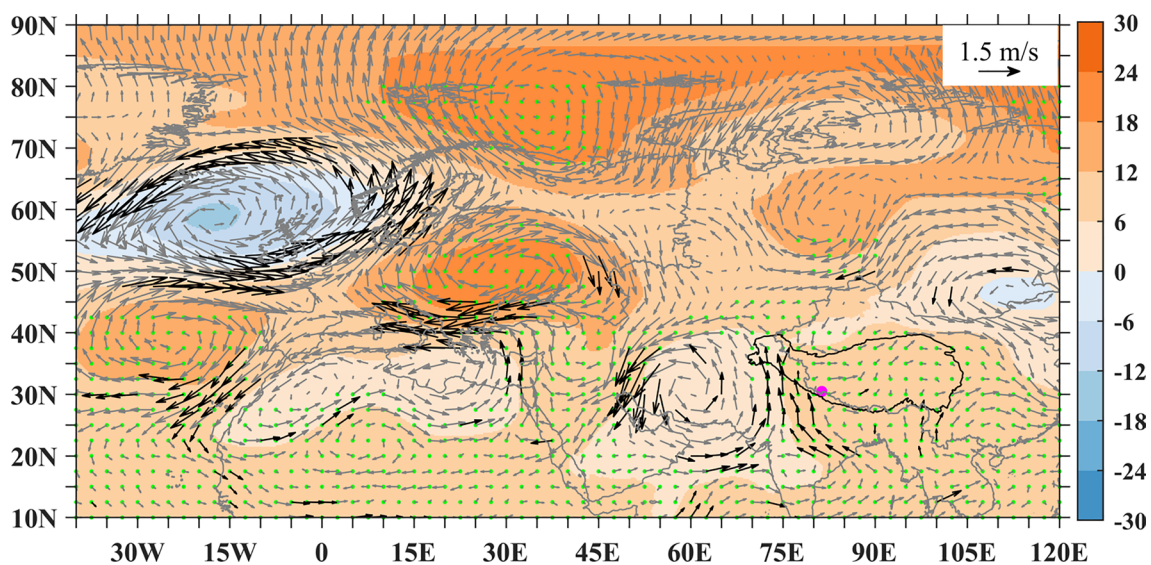


Figure 11. Differences in the mean 500 hPa geopotential heights (gpm) and wind speed field between the periods of 2000–2009 and 2010–2019 during the ablation season; the pink point indicates the location of Naimona'nyi Glacier; the 500 hPa geopotential heights and wind speed fields were from the ERA5 (Difference: 2010–2019 minus 2000–2009). The dotted areas (green dots) and black arrows indicated differences that are significant at the 0.1 level.

Table 2
Comparison of the Average Mass Balance on Naimona'nyi Glacier With That on Some Other Glaciers in the Himalayas Over the Last 10 Years

	Name	Max-Min	Mass balance (m w.e.)			Period	Origin
		Altitude	Annual	Cold	Ablation		
Western	Naimona'nyi	7,520–5,465	−0.44	−0.04	−0.4	2012/13–2016/17	This study
			−0.32	−0.03	−0.29	2010/11–2017/18	
	Chhota Shigri	5,830–4,072	−0.37	1.11	−1.49	2010/11–2017/18	Mandal et al. (2020)
	Stok	5,850–5,300	−0.47	0.71	−1.17	2010/11–2017/18	Soheb et al. (2020)
Central	Rikha Samba	6,515–5,416	−0.37			2011/12–2017/18	WGMS, 2020
	Mera	6,420–4,940	−0.28			2010/11–2017/18	WGMS, 2020
	Changri Nup	5,690–5,505	−1.52			2010/11–2017/18	WGMS, 2020
	Pokalde	5,660–5,580	−0.82			2010/11–2017/18	WGMS, 2020
	Yala	5,661–5,168	−0.85			2011/12–2017/18	WGMS, 2020
			−0.81	0.18	−0.98	2012/13–2016/17	Acharya et al. (2019)

train enhanced convection and southwest winds over the Indian subcontinent. The mean AMO in the ablation season was higher during the 2010–2019 period than that during the 2000–2009 period (Figure S7b). Thus, higher ablation-season precipitation from cyclonic anomaly over central India, which possibly link to enhanced convection over Indian subcontinent and the enhanced AMO, plays an important role in higher ablation-season mass balance for glaciers in the western Himalayas (especially for its east part) during the 2010–2019 period, relative to the 2000–2009 period. In summary, glaciers over most of the TP experienced increasing mass loss during the 2000–2019 period due to an increase in ablation-season T_a . The rate of mass loss slowed for glaciers in the western Himalayas over the last two decades, partly because of increase in cold-season precipitation and ablation-season precipitation that are linked to the changes in regional atmospheric circulation for different seasons.

5.3. Differences in Mass Balance Between Naimona'nyi Glacier and Other Himalayan Glaciers Over the Last Decade

In-situ measurements of glacier mass balance are available for several glaciers in the Himalayas (Wagnon et al., 2013; Zhao et al., 2016). A comparison of these measurements may lead to an increased understanding of the mechanisms that control spatial differences in the mass balance for glaciers over the Himalayas.

We first compared the average mass balance for Naimona'nyi Glacier with that for other glaciers in the western Himalayas during the 2011–2018 period (Table 2). The mean mass balance for Naimona'nyi Glacier during the 2011–2018 period was similar to that for Chhota Shigri and Stok glaciers. The average cold-season mass balance during the 2011–2018 period was significantly higher for Chhota Shigri and Stok glaciers than for Naimona'nyi Glacier due to higher cold-season precipitation for Chhota Shigri and Stok glaciers. The average ablation-season mass balance during the 2011–2018 period was significantly lower for Chhota Shigri and Stok glaciers than for Naimona'nyi Glacier because the former glaciers experienced higher T_a , cloudiness and humidity, resulting in higher melt energy from higher L_{in} , turbulent heat fluxes and lower snowfall (Table 2 and Table S7). Thus, the relatively high cold-season accumulation experienced by Chhota Shigri and Stok glaciers, and the relatively low ablation-season melt experienced by Naimona'nyi Glacier, resulted in a similar mean annual mass balance for the three glaciers.

We next compared the average mass balance for Naimona'nyi Glacier with that for some other glaciers on south-facing slopes in the central Himalayas during the 2011–2018 period. The mean mass balances for Changri Nup, Pokalde, and Yala glaciers were between 0.82 and 1.52 m w.e. a^{-1} lower than the mean mass balance for Naimona'nyi Glacier, which may be caused by lower mass balance during the ablation season on Changri Nup, Pokalde, and Yala glaciers (Table 2). Precipitation over south-facing slopes in the central Himalayas is significantly larger than at Naimona'nyi Glacier (Maussion et al., 2014). Thus, higher T_a , humidity

and cloudiness during the ablation season caused higher melt energy and lower mean annual mass balance on Changri Nup, Pokalde, and Yala glaciers, relative to Naimona'nyi Glacier.

In addition, there are some glaciers that have experienced relatively low mass loss on south-facing slopes in the central Himalayas. The mean mass balance for Mera and Rikha Samba glaciers during the 2011–2018 period is similar to our results for Naimona'nyi Glacier (Table 2). The relatively small mass balances for Mera and Rikha Samba glaciers may be related to high precipitation which compensated for mass loss from surface melt in the ablation season (Sherpa et al., 2017; Sunako et al., 2019). In summary, differences between the average mass balances for glaciers across the Himalayas over the last 10 years may be attributed to different local climate conditions, such as variations in the timing and amount of precipitation and T_a during the ablation season.

6. Conclusion

In this study, we have presented meteorological and glaciological observations for Naimona'nyi Glacier on a north-facing slope in the western Himalayas in the southwest TP from October 2010 to September 2018. These in-situ observations were used to run and calibrate the EMB model to analyze the energy and mass balance characteristics, and to assess which climate variables drive changes in the annual mass balance.

The in-situ measurements of glacier-wide mass balance for Naimona'nyi Glacier ranged from -0.9 to 0.23 m w.e.a⁻¹, with an average of -0.39 m w.e. a⁻¹. The mass balance was always negative at elevations below 6,070 m a.s.l. during the 2011–2018 period. Our sensitivity tests show that the present climate conditions make it unlikely that Naimona'nyi Glacier will achieve mass balance of zero. Our comparison of the average mass balance for Naimona'nyi Glacier with that for some other glaciers over the Himalayas during the 2011–2018 period shows that differences in the average annual mass balance over the last 10 years may be caused by differences in precipitation seasonality and amount of precipitation, and by T_a during the ablation season.

Simulations showed that that surface melt during the ablation season dominated the annual mass balance and the interannual variability in the mass balance, and that albedo controlled variations in melt energy during the ablation season. Compared to ablation-season T_a , the annual glacier-wide mass balance was controlled more by variations in annual precipitation during the 2011–2018 period. Precipitation during both the ablation season and the cold season had an impact on the changes in annual mass balance, mainly through its effect on albedo during the ablation season, which modified the ablation-season melt energy.

The average mass balance during the 2010–2019 period was lower than during the 2000–2009 period for glaciers in most regions on the TP and in the surrounding areas. This may be due to an increase in T_a during the ablation season, and/or a reduction in precipitation during the ablation season over the last two decades. However, the average glacier mass balance in the western Himalayas during the 2010–2019 period was higher than during the 2000–2009 period, partly due to an increase in annual precipitation during the 2010–2019 period which was driven by a change in regional atmospheric circulation. Over the last 20 years, the increased precipitation during the cold season was driven by an anomalous cyclonic circulation over the northwestern Indian Peninsula, which may be linked to the enhanced NAO in the cold season. And the increased precipitation during the ablation season over the last 20 years was driven by an anomalous cyclonic circulation over central India, which may be related to enhanced convection over the Indian subcontinent and the enhanced AMO.

Appendix A: Formulas in the Energy and Mass Balance Model

Daily albedo (α) contains snow albedo which is parameterized as a function of air temperature and humidity (Oerlemans & Knap, 1998), and ice albedo which is parameterized as a function of dew point temperature (Mölg et al., 2008). It is calculated as follows:

$$\alpha^{(i)} = \alpha_s^{(i)} + \left(\alpha_{\text{ice}} - \alpha_s^{(i)} \right) \exp\left(\frac{-d}{d^*} \right), \quad (\text{A1})$$

$$\alpha_s^{(i)} = \alpha_{\text{firm}} + (\alpha_{\text{firsnow}} - \alpha_{\text{firm}}) \exp\left(\frac{s-i}{t^*}\right), \quad (\text{A2})$$

$$\alpha_{\text{ice}} = \text{ice_a} * T_c + \text{ice_b}, \quad (\text{A3})$$

Where α_s is the fresh snow albedo; α_{ice} is the ice albedo; d is the snow depth (m); d^* is the characteristic scale for snow depth (m); α_{firm} is the firn albedo; s is the time since the last snowfall event; i is the actual time; t^* is time scale; ice_a and ice_b are constants; T_c is the dew point temperature. Because snow albedo will decrease more rapidly with time in wet conditions than in dry conditions, t^* was set as wet ($t1^*$) and dry ($t2^*$) conditions using surface temperature (Yang et al., 2013). Given that the relatively thin fresh snowpack probably melted away within a few hours in the ablation season, the snowfall threshold (Z_{th}) was introduced to determine whether fresh snowfall could persist through an entire daily cycle.

L_{in} is parameterized as a function of air temperature and humidity according to Duguay (1993).

$$L_{\text{in}} = \sigma(T_a + 273.15)^4 (b_1 + b_2 e_a), \quad (\text{A4})$$

where σ is the Stefan-Boltzmann constant ($5.67 \times 10^{-8} \text{ W m}^{-2} \text{ K}^{-4}$); T_a is the air temperature at the height of 2 m ($^{\circ}\text{C}$); e_a is the vapor pressure (h Pa) calculated from relative humidity and air temperature. The parameters of this L_{in} model were calibrated using the measured L_{in} , T_a , and RH at the Ngari Station for Desert Environment Observation and Research, Institute of Tibetan Plateau Research, Chinese Academy of Sciences, which is 350 km from Naimona'nyi Glacier (Figure 1a). The RMSE and r between the modeled and observed daily mean L_{in} were 15.3 W m^{-2} and 0.95 (Figure S2), respectively.

L_{out} is calculated by the Stefan-Boltzmann law from and surface emissivity (ϵ equal to 1) and surface temperature (T_s).

$$L_{\text{out}} = \epsilon \sigma (T_s + 273.15)^4. \quad (\text{A5})$$

T_s can be obtained using the same iterative calculations of Fujita and Ageta (2000).

H_{sen} and H_{lat} are calculated using the bulk method as follows:

$$H_{\text{sen}} = \rho_{\text{air}} c_p C_d u (T_a - T_s), \quad (\text{A6})$$

$$H_{\text{lat}} = \rho_{\text{air}} L_v C_d u (q_a - q_s), \quad (\text{A7})$$

where ρ_{air} is the density of air (kg m^{-3}); c_p is the specific heat of air ($1006 \text{ J kg}^{-1} \text{ K}^{-1}$); L_v is the latent heat of evaporation ($2.5 \times 10^6 \text{ J kg}^{-1}$) or sublimation ($2.83 \times 10^6 \text{ J kg}^{-1}$); C_d (0.002) is the bulk coefficient for sensible and latent heat; u is the wind speed (m s^{-1}) at the 2 m level; q_a and q_s is the specific humidity at the 2 m level and at the snow/ice surface, respectively.

The conductive heat flux (Q_G) in the subsurface was expressed according to the temperature profiles during a given time-span. The englacial snow/ice temperature (T_z) is solved from the conventional heat-conduction equation. Refreezing was composed of refrozen capillary water, refrozen water within cold snowpack, and superimposed ice. The detailed formulas can be seen in Fujita and Ageta (2000). Snowfall (P_{snow}) is calculated by daily precipitation (P) and two critical air-temperature thresholds for rain (T_{rain}) and snow (T_{snow}). When T_a is above (or below) T_{rain} (or T_{snow}), P_{snow} equals to zero (or P). Within these two temperature ranges, P_{snow} were calculated from linear interpolation with the following equation:

$$P_{\text{snow}} = \begin{cases} P & T \leq T_{\text{snow}} \\ \frac{T_{\text{rain}} - T}{T_{\text{rain}} - T_{\text{snow}}} P & T_{\text{snow}} < T < T_{\text{rain}} \\ 0 & T \geq T_{\text{rain}} \end{cases} \quad (\text{A8})$$

Data Availability Statement

Meteorological data from Burang meteorological station were downloaded from the China Meteorological Administration (<http://data.cma.cn/>). The NAO and AMO indexes were provided by the NOAA/OAR/ESRL PSD (<https://www.esrl.noaa.gov/psd/>). ERA5 reanalysis data sets are freely distributed on the Climate Date Store (<https://cds.climate.copernicus.eu/cdsapp#!/search?type=dataset>). Two automatic weather station data, monthly mean air temperature and relative humidity from two probes, and mass balance data for Naimona'nyi Glacier can be downloaded from the National Tibetan Plateau Data Center (<https://data.tpd.ac.cn/en/disallow/61857652-a35b-4e8c-b33b-e6bad6d1f377/>). Annual and seasonal mass balance data on Stok Glacier and meteorological data from Leh station were presented in Soheb et al. (2020). Annual mass balance data on Zhadang and Xiaodognkemadi glaciers was downloaded from the National Tibetan Plateau Data Center, Institute of Tibetan Research, Chinese Academy of Sciences (<https://data.tpd.ac.cn/en/data/8b1b1749-625e-46d9-a9f1-473fd96baff6/>). Annual and seasonal mass balance data on Chhota Shigri Glacier can be seen in Azam et al. (2014) and Mandal et al. (2020). Annual mass balance data on Rikha Samha, Mera, Changri Nup Pokalde and Ts. Tuyuksuyskiy glaciers and Urumqi Glacier No.1 can be downloaded from the world glacier monitoring service (<https://wgms.ch/ggcb/>). Annual and seasonal mass balance data on Yala Glacier were from Acharya et al. (2019). The SRTM data is provided by the US Geological Survey (<https://earthexplorer.usgs.gov/>).

Acknowledgments

This study is jointly funded by the Second Tibetan Plateau Scientific Expedition and Research Program (2019QZKK0201), the “Key Research Programs in Frontier Sciences” of the Chinese Academy of Sciences (grant QYZDY-SSW-DQC003), the Strategic Priority Research Program of Chinese Academy of Sciences (Grant XDA2006020102), National Natural Science Foundation of China (grants. 41771085, 41971092 and 41961134035), the National Science Foundation Paleo Perspectives on Climate Change (Award 1502919), National Key Research and Development Project (2019YFC1509102) and China Postdoctoral Science Foundation (grants 2018T110147 and 2017M611014).

References

- Acharya, A., & Kayastha, R. B. (2019). Mass and energy balance estimation of Yala glacier (2011–2017), Langtang valley, Nepal. *Water*, 11(1), 6. <https://doi.org/10.3390/w11010006>
- Azam, M. F., & Srivastava, S. (2020). Mass balance and runoff modelling of partially debris-covered Dokriani Glacier in monsoon-dominated Himalaya using ERA5 data since 1979. *Journal of Hydrology*, 590, 125432. <https://doi.org/10.1016/j.jhydrol.2020.125432>
- Azam, M. F., Wagnon, P., Vincent, C., Ramanathan, A., Linda, A., & Singh, V. B. (2014). Reconstruction of the annual mass balance of Chhota Shigri glacier, western Himalaya, India, since 1969. *Annals of Glaciology*, 55(66), 69–80. <https://doi.org/10.3189/2014aog66a104>
- Bolch, T., Kulkarni, A., Kääb, A., Huggel, C., Paul, F., Cogley, J. G., et al. (2012). The state and fate of Himalayan glaciers. *Science*, 336(6079), 310–314. <https://doi.org/10.1126/science.1215828>
- Bonekamp, P. N., de Kok, R. J., Collier, E., & Immerzeel, W. W. (2019). Contrasting meteorological drivers of the glacier mass balance between the Karakoram and central Himalaya. *Frontiers in Earth Science*, 7, 107. <https://doi.org/10.3389/feart.2019.00107>
- Bookhagen, B., & Burbank, D. W. (2010). Toward a complete Himalayan hydrological budget: Spatiotemporal distribution of snowmelt and rainfall and their impact on river discharge. *Journal of Geophysical Research*, 115, F03019. <https://doi.org/10.1029/2009jf001426>
- Brun, F., Berthier, E., Wagnon, P., Kääb, A., & Treichler, D. (2017). A spatially resolved estimate of High Mountain Asia glacier mass balances from 2000 to 2016. *Nature Geoscience*, 10(9), 668–673. <https://doi.org/10.1038/ngeo2999>
- Brun, F., Wagnon, P., Berthier, E., Jomelli, V., Maharjan, S. B., Shrestha, F., & Kraaijenbrink, P. D. A. (2019). Heterogeneous influence of glacier morphology on the mass balance variability in High Mountain Asia. *Journal of Geophysical Research: Earth Surf.*, 124(6), 1331–1345. <https://doi.org/10.1029/2018jfg004838>
- Carrivick, J. L., & Tweed, F. S. (2016). A global assessment of the societal impacts of glacier outburst floods. *Global and Planetary Change*, 144, 1–16. <https://doi.org/10.1016/j.gloplacha.2016.07.001>
- Dong, W., Lin, Y., Wright, J. S., Ming, Y., Xie, Y., Wang, B., et al. (2016). Summer rainfall over the southwestern Tibetan Plateau controlled by deep convection over the Indian subcontinent. *Nature Communications*, 7, 10925. <https://doi.org/10.1038/ncomms10925>
- Duguay, C. R. (1993). Radiation modeling in mountainous terrain review and status. *Mountain Research and Development*, 13(4), 339–357. <https://doi.org/10.2307/3673761>
- Forsythe, N., Fowler, H. J., Li, X.-F., Blenkinsop, S., & Pritchard, D. (2017). Karakoram temperature and glacial melt driven by regional atmospheric circulation variability. *Nature Climate Change*, 7, 664–670. <https://doi.org/10.1038/nclimate3361>
- Fujita, K., & Ageta, Y. (2000). Effect of summer accumulation on glacier mass balance on the Tibetan Plateau revealed by mass-balance model. *Journal of Glaciology*, 46(153), 244–252. <https://doi.org/10.3189/172756500781832945>
- Fujita, K., & Nuimura, T. (2011). Spatially heterogeneous wastage of Himalayan glaciers. *Proceedings of the National Academy of Sciences*, 108(34), 14011–14014. <https://doi.org/10.1073/pnas.1106242108>
- Giesen, R. H., van den Broeke, M. R., Oerlemans, J., & Andreassen, L. M. (2008). Surface energy balance in the ablation zone of Midtdalsbreen, a glacier in southern Norway: Interannual variability and the effect of clouds. *Journal of Geophysical Research*, 113, D21111. <https://doi.org/10.1029/2008jd010390>
- Guo, W., Liu, S., Xu, J., Wu, L., Shanguan, D., Yao, X., et al. (2015). The second Chinese glacier inventory: Data, methods, and results. *Journal of Glaciology*, 61(226), 357–372. <https://doi.org/10.3189/2015jog14j209>
- Hock, R., & Holmgren, B. (2005). A distributed surface energy-balance model for complex topography and its application to Storglaciären, Sweden. *Journal of Glaciology*, 51(172), 25–36. <https://doi.org/10.3189/172756505781829566>
- Hoffmann, L., Günther, G., Li, D., Stein, O., Wu, X., Griessbach, S., et al. (2019). From ERA-Interim to ERA5: The considerable impact of ECMWF's next-generation reanalysis on Lagrangian transport simulations. *Atmospheric Chemistry and Physics*, 19(5), 3097–3124. <https://doi.org/10.5194/acp-19-3097-2019>
- Huintjes, E. (2014). *Energy and mass balance modelling for glaciers on the Tibetan plateau: Extension, validation and application of a coupled snow and energy balance model (PhD thesis)*. RWTH Aachen University. Retrieved from <http://publications.rwth-aachen.de/record/459462>
- Immerzeel, W. W., Lutz, A. F., Andrade, M., Bahl, A., Biemans, H., Bolch, T., et al. (2020). Importance and vulnerability of the world's water towers. *Nature*, 577(7790), 364–369. <https://doi.org/10.1038/s41586-019-1822-y>

- Kehrwald, N. M., Thompson, L. G., Tandong, Y., Mosley-Thompson, E., Schotterer, U., Alfimov, V., et al. (2008). Mass loss on Himalayan glacier endangers water resources. *Geophysical Research Letters*, *35*(22). <https://doi.org/10.1029/2008gl035556>
- Kenzhebaev, R., Barandun, M., Kronenberg, M., Chen, Y., Usabaliev, R., & Hoelzle, M. (2017). Mass balance observations and reconstruction for Batysh Sook Glacier, Tien Shan, from 2004 to 2016. *Cold Regions Science and Technology*, *135*, 76–89. <https://doi.org/10.1016/j.coldregions.2016.12.007>
- King, O., Dehecq, A., Quincey, D., & Carrivick, J. (2018). Contrasting geometric and dynamic evolution of lake and land-terminating glaciers in the central Himalaya. *Global and Planetary Change*, *167*, 46–60. <https://doi.org/10.1016/j.gloplacha.2018.05.006>
- Li, S., Yao, T., Yu, W., Yang, W., & Zhu, M. (2019). Energy and mass balance characteristics of the Guliya ice cap in the west Kunlun Mountains, Tibetan Plateau. *Cold Regions Science and Technology*, *159*, 71–85. <https://doi.org/10.1016/j.coldregions.2018.12.001>
- Liu, Q., & Liu, S. (2016). Response of glacier mass balance to climate change in the Tianshan mountains during the second half of the twentieth century. *Climate Dynamics*, *46*(1–2), 303–316. <https://doi.org/10.1007/s00382-015-2585-2>
- Liu, X., Liu, Y., Wang, X., & Wu, G. (2020). Large-scale dynamics and moisture sources of the precipitation over the western Tibetan Plateau in boreal winter. *Journal of Geophysical Research: Atmosphere*, *125*, e2019JD032133. <https://doi.org/10.1029/2019jd032133>
- Mandal, A., Ramanathan, A., Azam, M. F., Angchuk, T., Soheb, M., Kumar, N., et al. (2020). Understanding the interrelationships among mass balance, meteorology, discharge and surface velocity on Chhota Shigri Glacier over 2002–2019 using in situ measurements. *Journal of Glaciology*, *66*(259), 727–741. <https://doi.org/10.1017/jog.2020.42>
- Maurer, J. M., Schaefer, J. M., Rupper, S., & Corley, A. (2019). Acceleration of ice loss across the Himalayas over the past 40 years. *Science Advance*, *5*(6), eaav7266. <https://doi.org/10.1126/sciadv.aav7266>
- Ménard, C. B., Essery, R., Barr, A., Bartlett, P., Derry, J., Dumont, M., et al. (2019). Meteorological and evaluation datasets for snow modelling at 10 reference sites: Description of in situ and bias-corrected reanalysis data. *Earth System Science Data*, *11*(2), 865–880. <https://doi.org/10.5194/essd-11-865-2019>
- Mölg, T., Cullen, N. J., Hardy, D. R., Kaser, G., & Klok, L. (2008). Mass balance of a slope glacier on Kilimanjaro and its sensitivity to climate. *International Journal of Climatology*, *28*(7), 881–892. <https://doi.org/10.1002/joc.1589>
- Mölg, T., Maussion, F., & Scherer, D. (2014). Mid-latitude westerlies as a driver of glacier variability in monsoonal high Asia. *Nature Climate Change*, *4*(1), 68–73. <https://doi.org/10.1038/nclimate2055>
- Oerlemans, J., Anderson, B., Hubbard, A., Huybrechts, P., Jóhannesson, T., Knap, W. H., et al. (1998). Modelling the response of glaciers to climate warming. *Climate Dynamics*, *14*(4), 267–274. <https://doi.org/10.1007/s003820050222>
- Oerlemans, J., & Balkema, A. A. (2001). *Glaciers and climate change*. Brookfield, Vt. CRC Press.
- Oerlemans, J., & Knap, W. H. (1998). A 1 year record of global radiation and albedo in the ablation zone of Morteratschgletscher, Switzerland. *Journal of Glaciology*, *44*(147), 231–238. <https://doi.org/10.1017/s0022143000002574>
- Qiu, T., Huang, W., Wright, J. S., Lin, Y., Lu, P., He, X., et al. (2019). Moisture sources for wintertime intense precipitation events over the three snowy subregions of the Tibetan Plateau. *Journal of Geophysical Research: Atmospheres*, *124*(23), 12708–12725. <https://doi.org/10.1029/2019jd031110>
- Ragetelli, S., Pellicciotti, F., Bordoy, R., & Immerzeel, W. W. (2013). Sources of uncertainty in modeling the glaciological response of a Karakoram watershed to climate change. *Water Resources Research*, *49*, 6048–6066. <https://doi.org/10.1002/wrcr.20450>
- Reijmer, C. H., & Hock, R. (2008). Internal accumulation on Storglaciären, Sweden, in a multi-layer snow model coupled to a distributed energy- and mass-balance model. *Journal of Glaciology*, *54*(184), 61–72. <https://doi.org/10.3189/002214308784409161>
- Sakai, A., & Fujita, K. (2017). Contrasting glacier responses to recent climate change in high-mountain Asia. *Scientific Reports*, *7*, 13717. <https://doi.org/10.1038/s41598-017-14256-5>
- Sakai, A., Nuimura, T., Fujita, K., Takenaka, S., Nagai, H., & Lamsal, D. (2015). Climate regime of Asian glaciers revealed by GAMDAM glacier inventory. *The Cryosphere*, *9*, 865–880. <https://doi.org/10.5194/tc-9-865-2015>
- Scherler, D., Bookhagen, B., & Strecker, M. R. (2011). Spatially variable response of Himalayan glaciers to climate change affected by debris cover. *Nature Geoscience*, *4*(3), 156–159. <https://doi.org/10.1038/ngeo1068>
- Shean, D. E., Bhushan, S., Montesano, P., Rounce, D. R., Arendt, A., & Osmanoglu, B. (2020). A systematic, regional assessment of high mountain Asia glacier mass balance. *Frontiers in Earth Science*, *7*, 363. <https://doi.org/10.3389/feart.2019.00363>
- Sherpa, S. F., Wagnon, P., Brun, F., Berthier, E., Vincent, C., Lejeune, Y., et al. (2017). Contrasted surface mass balances of debris-free glaciers observed between the southern and the inner parts of the Everest region (2007–15). *Journal of Glaciology*, *63*(240), 637–651. <https://doi.org/10.1017/jog.2017.30>
- Shi, Y., & Liu, S. (2000). Estimation on the response of glaciers in China to the global warming in the 21st century. *Chinese Science Bulletin*, *45*(7), 668–672. <https://doi.org/10.1007/bf02886048>
- Soheb, M., Ramanathan, A., Angchuk, T., Mandal, A., Kumar, N., & Lotus, S. (2020). Mass-balance observation, reconstruction and sensitivity of Stok glacier, Ladakh region, India, between 1978 and 2019. *Journal of Glaciology*, *66*(258), 627–642. <https://doi.org/10.1017/jog.2020.34>
- Sunako, S., Fujita, K., Sakai, A., & Kayastha, R. B. (2019). Mass balance of Trambau Glacier, Rolwaling region, Nepal Himalaya: In-situ observations, long-term reconstruction and mass-balance sensitivity. *Journal of Glaciology*, *65*(252), 605–616. <https://doi.org/10.1017/jog.2019.37>
- Sun, J., Yang, K., Guo, W., Wang, Y., He, J., & Lu, H. (2020). Why has the inner Tibetan Plateau become wetter since the mid-1990s? *Journal of Climate*, *33*(19), 8507–8522. <https://doi.org/10.1175/jcli-d-19-0471.1>
- Thibert, E., Blanc, R., Vincent, C., & Eckert, N. (2008). Glaciological and volumetric mass-balance measurements: Error analysis over 51 years for Glacier de Sarennes, French Alps. *Journal of Glaciology*, *54*(186), 522–532. <https://doi.org/10.3189/002214308785837093>
- Thompson, L. G., Mosley-Thompson, E., Davis, M. E., & Brecher, H. H. (2011). Tropical glaciers, recorders and indicators of climate change, are disappearing globally. *Annals of Glaciology*, *52*(59), 23–34. <https://doi.org/10.3189/172756411799096231>
- Tian, L., Zong, J., Yao, T. Y., Ma, L. M., Pu, J. P., & Zhu, D. (2014). Direct measurement of glacier thinning on the southern Tibetan Plateau (Gurenhekou, Kangwure and Naimona'nyi glaciers). *Journal of Glaciology*, *60*(223), 879–888. <https://doi.org/10.3189/2014JoG14J022>
- Vatsal, F., Scherer, D., Mölg, T., Collier, E., Curio, J., & Finkelnburg, R. (2014). Precipitation seasonality and variability over the Tibetan Plateau as resolved by the high Asia reanalysis. *Journal of Climate*, *27*(5), 1910–1927. <https://doi.org/10.1175/jcli-d-13-00282.1>
- Vincent, C., Ramanathan, A., Wagnon, P., Dobhal, D. P., Linda, A., Berthier, E., et al. (2013). Balanced conditions or slight mass gain of glaciers in the Lahaul and Spiti region (northern India, Himalaya) during the nineties preceded recent mass loss. *The Cryosphere*, *7*(2), 569–582. <https://doi.org/10.5194/tc-7-569-2013>
- von Engel, A., & Teixeira, J. (2013). A planetary boundary layer height climatology derived from ECMWF reanalysis data. *Journal of Climate*, *26*(17), 6575–6590. <https://doi.org/10.1175/jcli-d-12-00385.1>

- Wagnon, P., Vincent, C., Arnaud, Y., Berthier, E., Vuillermoz, E., Gruber, S., et al. (2013). Seasonal and annual mass balances of Mera and Pokalde glaciers (Nepal Himalaya) since 2007. *The Cryosphere*, 7, 1769–1786. <https://doi.org/10.5194/tc-7-1769-2013>
- Wang, N., Wu, H., Wu, Y., & Chen, A. (2015). Variations of the glacier mass balance and lake water storage in the Tarim basin, northwest China, over the period of 2003–2009 estimated by the ICESat-GLAS data. *Environment Earth Science*, 74(3), 1997–2008. <https://doi.org/10.1007/s12665-015-4662-6>
- WGMS (2020). Global Glacier Change Bulletin No. 3 (2016-2017). In M. Zemp, I. Gärtner-Roer, S. U. Nussbaumer, J. Bannwart, P. Rastner, F. Paul, & M. Hoelzle (Eds.), *ISC(WDS)/IUGG(IACS)/UNEP/UNESCO/WMO*. Zurich, Switzerland: World Glacier Monitoring Service. Retrieved from <https://doi.org/10.5904/wgms-fog-2019-12>
- Yadav, R. K., Rupa Kumar, K., & Rajeevan, M. (2009). Increasing influence of ENSO and decreasing influence of AO/NAO in the recent decades over northwest India winter precipitation. *Journal of Geophysical Research*, 114(D12). <https://doi.org/10.1029/2008jd011318>
- Yang, K., He, J., Tang, W., Qin, J., & Cheng, C. C. K. (2010). On downward shortwave and longwave radiations over high altitude regions: Observation and modeling in the Tibetan Plateau. *Agricultural and Forest Meteorology*, 150(1), 38–46. <https://doi.org/10.1016/j.agrformet.2009.08.004>
- Yang, W., Guo, X., Yao, T., Zhu, M., & Wang, Y. (2016). Recent accelerating mass loss of southeast Tibetan glaciers and the relationship with changes in macroscale atmospheric circulations. *Climate Dynamics*, 47(3–4), 805–815. <https://doi.org/10.1007/s00382-015-2872-y>
- Yang, W., Yao, T., Guo, X., Zhu, M., Li, S., & Kattel, D. B. (2013). Mass balance of a maritime glacier on the southeast Tibetan Plateau and its climatic sensitivity. *Journal of Geophysical Research: Atmospheres*, 118(17), 9579–9594. <https://doi.org/10.1002/jgrd.50760>
- Yao, T. (2018). *Dataset of typical glacier changes on Tibetan Plateau and Its surrounding areas (2005–2016)*. National Tibetan Plateau Data Center. Retrieved from <https://doi.org/10.11888/GlaciologyGeocryology.tpe.96.db>
- Yao, T., Masson-Delmotte, V., Gao, J., Yu, W., Yang, X., Risi, C., et al. (2013). A review of climatic controls on $\delta^{18}\text{O}$ in precipitation over the Tibetan Plateau: Observations and simulations. *Reviews of Geophysics*, 51(4), 525–548. <https://doi.org/10.1002/rog.20023>
- Yao, T., Thompson, L., Yang, W., Yu, W., Gao, Y., Guo, X., et al. (2012). Different glacier status with atmospheric circulations in Tibetan Plateau and surroundings. *Nature Climate Change*, 2(9), 663–667. <https://doi.org/10.1038/nclimate1580>
- Yao, T., Yu, W., Wu, G., Xu, B., Yang, W., Zhao, H., et al. (2019). Glacier anomalies and relevant disaster risks on the Tibetan Plateau and surroundings. *Chinese Science Bulletin*, 64(27), 2770–2782. <https://doi.org/10.1360/TB-2019-0246>
- Zhang, H., Li, Z., Zhou, P., Zhu, X., & Wang, L. (2018). Mass-balance observations and reconstruction for Haxilegen Glacier No.51, eastern Tien Shan, from 1999 to 2015. *Journal of Glaciology*, 64(247), 689–699. <https://doi.org/10.1017/jog.2018.58>
- Zhang, Y., Hirabayashi, Y., & Liu, S. (2012). Catchment-scale reconstruction of glacier mass balance using observations and global climate data: Case study of the Hailuoguo catchment, south-eastern Tibetan Plateau. *Journal of Hydrology*, 444–445, 146–160. <https://doi.org/10.1016/j.jhydrol.2012.04.014>
- Zhao, H., Yang, W., Yao, T., Tian, L., & Xu, B. (2016). Dramatic mass loss in extreme high-elevation areas of a western Himalayan glacier: Observations and modeling. *Scientific Reports*, 6, 30706. <https://doi.org/10.1038/srep30706>
- Zhu, D., Tian, L., Wang, J., Wang, Y., & Cui, J. (2014). Rapid glacier retreat in the Naimona'nyi region, western Himalayas, between 2003 and 2013. *Journal of Applied Remote Sensing*, 8(1), 083508. <https://doi.org/10.1117/1.jrs.8.083508>
- Zhu, M., Yao, T., Xie, Y., Xu, B., Yang, W., & Yang, S. (2020). Mass balance of Muji Glacier, northeastern Pamir, and its controlling climate factors. *Journal of Hydrology*, 590, 125447. <https://doi.org/10.1016/j.jhydrol.2020.125447>
- Zhu, M., Yao, T., Yang, W., Maussion, F., Huintjes, E., & Li, S. (2015). Energy- and mass-balance comparison between Zhadang and Parlung No. 4 glaciers on the Tibetan Plateau. *Journal of Glaciology*, 61(227), 595–607. <https://doi.org/10.3189/2015jog14j206>
- Zhu, M., Yao, T., Yang, W., Xu, B., Wu, G., & Wang, X. (2018). Differences in mass balance behavior for three glaciers from different climatic regions on the Tibetan Plateau. *Climate Dynamics*, 50(9–10), 3457–3484. <https://doi.org/10.1007/s00382-017-3817-4>
- Zhu, M., Yao, T., Yang, W., Xu, B., Wu, G., Wang, X., & Xie, Y. (2018). Reconstruction of the mass balance of Muztag Ata No. 15 glacier, eastern Pamir, and its climatic drivers. *Journal of Glaciology*, 64(244), 259–274. <https://doi.org/10.1017/jog.2018.16>

Reference From the Supporting Information

- RGI Consortium. (2017). *Randolph Glacier Inventory – a dataset of global glacier outlines: Version 6.0: Technical report, global land ice measurements from space*. Colorado, USA: Digital Media. Retrieved from <https://doi.org/10.7265/N5-RGI-60>
- Zhu, M., Yao, T., Yang, W., Xu, B., & Wang, X. (2017). Evaluation of parameterizations of incoming longwave radiation in the high-mountain region of the Tibetan Plateau. *Journal of Applied Meteorology and Climatology*, 56(4), 833–848. <https://doi.org/10.1175/jamc-d-16-0189.1>